HAL
open science

Internal structures and dating of non-sulphide Zn deposits 5 using rock magnetism: insights from the Moroccan High Atlas

Nicolas Charles, Flavien Choulet, Stanislas Sizaret, Yan Chen, Luc Barbanson, Aomar Ennaciri, Lakhlifi Badra, Yannick Branquet

To cite this version:

Nicolas Charles, Flavien Choulet, Stanislas Sizaret, Yan Chen, Luc Barbanson, et al.. Internal structures and dating of non-sulphide Zn deposits 5 using rock magnetism: insights from the Moroccan High Atlas. Mineralium Deposita, 2016, 51 (1), pp.151-175. 10.1007/s00126-015-0596-x . insu-01164517

HAL Id: insu-01164517

https://insu.hal.science/insu-01164517v1

Submitted on 26 Jun 2015

HAL is a multi-disciplinary open access archive for the deposit and dissemination of scientific research documents, whether they are published or not. The documents may come from teaching and research institutions in France or abroad, or from public or private research centers.

L'archive ouverte pluridisciplinaire **HAL**, est destinée au dépôt et à la diffusion de documents scientifiques de niveau recherche, publiés ou non, émanant des établissements d'enseignement et de recherche français ou étrangers, des laboratoires publics ou privés.

Manuscript
Click here to download Manuscript: Text_revised.docx

Internal structures and dating of non-sulphide Zn deposits using rock magnetism: Insights from the Moroccan High-Atlas

Nicolas CHARLES[1,*], Flavien CHOULET[2], Stanislas SIZARET[3], Yan CHEN[3], Luc BARBANSON[3], Aomar ENNACIRI[4], Lakhlifi BADRA[5], Yannick BRANQUET[3].

1: Bureau de Recherches Géologiques et Minières (BRGM-French Geological Survey), Orléans, France

2: Université de Franche-Comté, UMR-CNRS 6249 Chrono-Environnement, Besançon, France

3: Institut des Sciences de la Terre d'Orléans, UMR 7327-CNRS/Université d'Orléans/BRGM, Orléans, France

4: Groupe Managem, Casablanca, Morocco

5: Université Moulay Ismaïl, Meknès, Morocco

Abstract

The renewal of interest in Zn-Pb non-sulphide ores has been induced by mineral processing improvement and leads to new exploration and mining projects in the world. Although the mineralogy is often precisely known, and despite several studies linking ore deposition to regional tectonics, absolute dating of non-sulphide stages is rare and structure of ore bodies was largely disregarded. Geochronological data from non-sulphide ores are essential to timely constrain alteration episodes and to insert supergene ore genesis in the climate and tectonic evolution of the metallogenic province. The access to internal organisation of ore could reveal post-mineralization episodes related to supergene evolution. Thus, a rock magnetism study combining Anisotropy of Magnetic Susceptibility (AMS) and palaeomagnetism was performed on four non-sulphide deposits from the Moroccan High-Atlas. AMS generally shows similar horizontal magnetic fabrics for ores and the clayey and carbonaceous internal sediments filling karstic cavities. The palaeomagnetic directions of ores and internal sediments are compatible and the calculated poles are consistent with the last 30

Ma of the Africa Apparent Polar Wander Path, with an upper age at 0.78 Ma. The proposed three-step scenario is placed within the evolution of the Moroccan High-Atlas belt. Deposition of primary sulphides is contemporaneous with opening of the Tethyan and Atlantic oceans. During the Tertiary, intracontinental deformation gave rise to the High-Atlas fold-and-thrust belt and to regional uplift. Finally, Zn-Pb sulphides, hosted in carbonates experienced oxidation under an arid climate to form karst-related Zn-Pb non-sulphide ores. These promising results pave the way for an efficient method to constrain the internal fabrics and age of Zn supergene deposits.

Key-words: non-sulphide Zn deposit, AMS, palaeomagnetism, dating, High-Atlas, Morocco.

*Corresponding author: n.charles@brgm.fr

1. Introduction

Non-sulphide zinc ores, also called “calamines” or “zinc oxides” were the main sources of zinc metal until the end of the nineteenth century (e.g. Large 2001; Boni et al. 2003; Hitzman et al. 2003). New processing technologies, such as hydrometallurgical acid-leaching, solvent extraction (SX) and electro-winning techniques (Cole and Sole 2002; Gnoinski 2007; Hosseini 2008), recently lead to a regain of interest in non-sulphide Zn-Pb ores with exploration and mining projects in Iran (Daliran et al. 2009; 2013), Namibia (Borg et al. 2003), Zambia (Terraciano 2008), Turkey (Santoro et al. 2013) and Peru (Boni et al. 2009). In non-sulphide Zn ores, zinc occurs as a major component of carbonates (smithsonite), silicates (willemite), hydrated minerals (Zn-clays, hemimorphite, hydrozincite) and minor phases listed in Hitzman et al. (2003). Based on physico-chemical conditions for

mineral occurrence, hypogene and supergene deposits have been distinguished (Heyl and Bozion 1962; Large 2001; Hitzman et al. 2003). Only supergene deposits will be discussed in this article.

During the last decade, many efforts have been made on understanding metallogeny of non-sulphide zinc deposits. Research has focused on describing the different zinc-bearing minerals (e.g. Borg et al. 2003; Boni et al. 2009; Daliran et al. 2009) and identifying the physico-chemical conditions they were formed (e.g. Boni et al. 2003; Reichert and Borg 2008; Choulet et al. 2014). Although the succession of mineral assemblages is often known in detail, absolute dating of non-sulphide stages is rare and limited to particular geochronometers such as Rb/Sr on willemite or clay (Schneider et al. 2008), U/Th-He on zinc vanadate (Boni et al. 2007) or Ar/Ar on zinc-lead manganese oxide (Groves et al. 2003). Obtaining geochronological data from non-sulphide mineralogical assemblage are essential to timely constrain oxidation episodes and to insert supergene ore genesis in the climate and tectonic evolution of the metallogenic province. In addition, despite several studies linking ore deposition to regional tectonics (Borg 2003; 2009), the structure of ore bodies was largely disregarded, as a consequence of the intricate supergene processes involved in karst-related deposits, where multiple weathering episodes and evolution of the hydrodynamics have contributed to successive chemical and mechanical reworking, respectively (Boni et al. 2003). Therefore, macroscopic and microscopic observations are often not sufficient to decipher the ore internal structure. To image these fabrics, it is possible to recourse to magnetic properties of minerals and especially to anisotropy of the magnetic susceptibility (AMS). This tool may provide information on the internal organisation of ore and can be used to reveal post-mineralization episodes related to supergene evolution (e.g. Essalhi et al. 2009). When geochronometer minerals are absent, the approach of palaeomagnetism can be also useful to indirectly constrain the age of mineralization. These methods have been successfully applied

to various types of deposits like VMS gossan (Essalhi et al. 2011), MVT (Symons et al. 1996; 2002), and iron laterites (Théveniaut and Freyssinet 1999; 2002; Théveniaut et al. 2007; Ricordel-Prognon et al. 2010). Boni et al. (2005) attempted dating of non-sulphide Zn-Pb ores of SW Sardinia (Italy) by palaeomagnetism. Despite scarce sampling and non-conclusive results, the authors suggested that this method can be effective to constrain the timing of oxidation in supergene-enriched ores, representing an interesting methodological challenge with multiple possible targets throughout the world.

This contribution aims at showing that rock magnetism properties may be used to constrain age and geometry in supergene ore deposits, with the example of the Moroccan zinc non-sulphide deposits. The Moroccan High Atlas is an intracontinental Cenozoic belt that exposes numerous supergene Zn non-sulphide deposits hosted in the Lower Jurassic limestone (**Figure 1**). Choulet et al. (2014) studied the mineralogical assemblage of six deposits and identified a direct replacement of Zn-Pb sulphides by carbonates and silicates, accompanied by precipitation of Zn non-sulphide minerals in cavities with internal karstic sedimentary filling. Based on field observations, they proposed that formation of the non-sulphide ore is coeval with Atlas deformation and uplift during the Cenozoic. Therefore this area represents a good target to use palaeomagnetism to timely constrain the supergene oxidation episodes. We have selected four localities (Aït Labbès, Toulal, Beni Tajite and Tadaghast; **Figure 1**) and collected samples from both veins of non-sulphide Zn ore and cavities filled by internal karstic sediments. After a careful study of the mineralogy to identify the magnetic carriers, we present AMS and palaeomagnetism results that allow us to discuss the internal structure of the mineralized body and its age in the general framework of the Atlas tectonic and climate evolution.

2. Geological and metallogenetic setting

2.1. The Moroccan High-Atlas

The Atlas Mountains is an intracontinental orogen, WSW-ENE trending mountain belts, extending from Morocco to Tunisia (e.g. Frizon de Lamotte et al. 2009 and references therein; **Figure 1a**). The Moroccan High-Atlas is composed of Mesozoic to Cenozoic sedimentary rocks overlying on a Precambrian to Palaeozoic basement (**Figures 1b and 1c**), deformed during the Variscan orogeny (Mattauer et al. 1977; Piqué and Michard 1989). According to Laville and Piqué (1991), inheritance of Palaeozoic structures largely constrains the geometry of the Mesozoic rifting episode related to the opening of the Tethys and the Atlantic Ocean. The sedimentary pile comprises from bottom to the top: 1) Triassic detrital rocks, evaporites (du Dresnay 1988; Piqué 1994) associated with mafic volcanics lava, 2) Lower to Middle Jurassic marl, limestone and calcareous turbidite, and 3) upper Middle Jurassic continental red beds (Charrière et al. 2005) with contemporaneous magmatism (Brechbühler et al. 1988; Laville and Piqué 1992). Sedimentation resumed with Cretaceous red sandstone and limestone deposits. The Late Cretaceous carbonate platform marks a short but major Late Cenomanian-Turonian transgression event (Haddoumi et al. 2008), since continental sedimentation is recorded again at the end of Cretaceous, during the Palaeocene (Charrière et al. 2009) and until the mid-Eocene (Herbig and Trappe 1994).

Presently, the Moroccan High-Atlas exhibits a fold-and-thrust bulk architecture that results from inversion tectonics of the former Mesozoic extensional basins, controlled by NE-SW trending normal faults (Laville et al. 2004; Frizon de Lamotte et al. 2008). The NE-SW strike of the faults is slightly oblique to the general ENE-WSW trend of the belt (**Figure 1a**). Lower to Middle Jurassic strata are found in the wide and open synclines, while anticlines are comparatively narrow and are underlined by thick Lower Jurassic limestone ridges (**Figure**

1c). Locally, the anticline hinges are affected by thrusting, exposing the underlying Triassic strata that form the décollement layer. The formation of the intracontinental belt in the Moroccan High-Atlas (Mattauer et al. 1977) has been facilitated by the inherited crustal weaknesses due to Mesozoic rifting. Although the chronology of faulting and uplift is still disputed, inversion tectonics of the Triassic to Jurassic normal faults occurred between Eocene and Quaternary, with alternation of quiet and active periods of uplift (Frizon de Lamotte et al. 2009). While compression chiefly occurs at the Lutetian-Bartonian transition (ca. 40 Ma), a secondary Pleistocene episode has caused the present topography of the range.

The Lower Jurassic carbonate massif of the Moroccan High Atlas has experienced intense karstification driven by 1) the tectonic structures relative to Tertiary tectonics, and 2) the lithology, with a preferred development of karst network in reef limestone and dolostone (Couvreur, 1978). Several episodes of karst development have been recorded in the literature: 1) an early stage (Lower Jurassic) coeval with sulphide deposition is recorded at Beni Tajite deposit (Choulet et al. 2014), a Cretaceous event during a major emersion phase (Subra, 1980), post-Eocene to Mio-Pliocene episodes related to the Atlas tectonics and exhumation of the Jurassic rocks (Bouchaou, 1988), and Pliocene to Quaternary evolution (Nicod, 1997) driven by the reactivation of Atlas faults.

2.2. Non-sulphide Zn-Pb deposits of Moroccan High-Atlas

The numerous Zn-Pb ore deposits in Northern Africa belong to the Zn-Pb province of the circum-Mediterranean Sea and Alpine Europe (Rouvier et al. 1985), a wide area of economic interest for the extraction of base metals (Emberger 1969; Popov 1968; Decrée et al. 2008; 2010; Bruyère et al. 2010; Jemmali et al. 2011). In the Moroccan High-Atlas, Zn-Pb ore deposits occur throughout the belt (**Figure 1b**). Two main metallogenic periods have been

recognized for Zn-Pb sulphide ore deposition (Mouguina 2004): (1) the Lower Jurassic period, with stratabound lenses of Zn-Pb-Fe sulphides considered as syngenetic (Agard and du Dresnay 1965; Emberger 1965; Bazin 1968; Auajjar and Boulègue 1999); (2) the Middle Jurassic (i.e. Dogger) period, characterized by Cu-Ni and Zn-Pb ore deposits spatially and temporally associated to mafic magmas, and to reactivated faults (Caïa 1968; Chèvremont 1975).

In the Moroccan High-Atlas, Zn-Pb mineralization often consists of non-sulphide zinc ores, locally called "calamines" (Ovtracht 1978), which are considered to result from the supergene alteration of a primary carbonate-hosted sulphide protore (Agard and du Dresnay 1965; Bazin 1968; Leblanc 1968; Mouguina 2004). The origin of primary sulphides (Sedex or MVT types) is not clearly established yet and is beyond the scope of this paper. Based on field and mineralogical studies of six non-sulphide Zn-Pb deposits, Choulet et al. (2014) recently published a new model to explain the formation of Moroccan High-Atlas non-sulphide ore deposits. They recognized two superimposed stages of weathering, following the formation of the protore sulphides (themselves more or less coeval with deposition of Lower Jurassic host limestone):

- (1) early supergene weathering with formation of Zn-Pb carbonates and iron oxi-hydroxides,
- (2) late supergene weathering with deposition of Zn-carbonates, Zn-silicates and hydrated phases.

The proposed scenario falls within the tectonic evolution of the Moroccan High Atlas belt. Deposition of primary sulphides is contemporaneous with opening of the Tethyan and Atlantic oceans. During the Tertiary, intracontinental deformation has given rise to the High Atlas fold-and- thrust belt and to regional uplift. As a result, Zn–Pb sulphides, hosted in carbonates experienced oxidation under an arid climate to form karst-related Zn–Pb non-

sulphide ore bodies. Our good understanding of processes involved and the well-established chronology allow us to study, rock magnetism to constrain the ore body structure and its formation age by means of magnetic fabrics and palaeomagnetism, respectively. Despite this complex weathering evolution, iron-bearing phases representing the main magnetic carriers, are formed during the early supergene event and not reworked by the late one, apparently preventing remagnetization.

2.3. The Tadaghast, Aït Labbès, Toulal and Beni Tajite ore deposits

In this study, four occurrences and deposits have been investigated: Tadaghast, Aït Labbès, Toulal and Beni Tajite (**Figure 1b**). The geological setting has been extensively studied by Choulet et al. (2014). Only a brief outline of macroscopic and microscopic observations is provided here (Figures 2 and 3), and the reader can refer to Choulet et al. (2014) and references therein for a more detailed description.

In the field, non-sulphide Zn-Pb deposits are often associated to tightly faulted anticlines (**Figure 2a**), except for the tabular series that hosts the Beni Tajite ore deposit (Agard and du Dresnay 1965). Non-sulphide ores are always hosted in Lower Jurassic limestone formed in a reefal or para-reefal environment commonly close to the transition from the platform to the deep sea (du Dresnay 1979; Leblanc 1968). Mineralized system is associated to a karst-related network formed after tectonic features and exposing dissolution cavities in the limestone, as well exemplified at Toulal and Aït Labbès sites (**Figures 2b, 2c and 2d**).

The protore mainly consists of stratabound lenses of primary sulphides (galena, sphalerite and pyrite; **Figure 3a**) and massive white calcite. Superimposed supergene oxidation includes the formation of non-sulphide Zn-Pb minerals and iron oxi-hydroxides

(e.g. smithsonite, hemimorphite, hydrozincite, goethite, hematite; **Figures 2e and 2g**). Two successive types of non-sulphide ores have been observed all over the studied sites (Choulet et al. 2014; **Figures 2h and 2i**):

- a red ore (locally called red calamine) composed of the iron oxi-hydroxides-smithsonite association (**Figures 2h, 3b and 3c**); in all samples dissolved pyrite are replaced by zoned goethite and hematite (Choulet et al. 2014).

- a "grey to white ore" (locally called grey or white calamine) superimposed on the red type or precipitated in karst cavities with limited metal transport (**Figures 2i and 3d**). It is worth to notice that no iron oxi-hydroxides are involved in this second stage.

Besides, the development of the karst network within limestone host-rocks implies internal sedimentation, as evidenced by horizontally bedding within up to 10 meters scale cavities (**Figure 2f**). Locally, the horizontal bedding is disturbed due to either sedimentary processes or post-deposition tectonics. Although interference between karst formation and supergene evolution of ore may occur, internal sediments are usually Zn-poor (grading 4-5 ZnO wt.%, Choulet et al., 2014), and mainly made up of marl and calcareous shale including clasts of calamine and iron (hydr-)oxides (**Figures 3e and 3f**). Laminated internal sediments display micrometric to centimetric alternations of banded calcite and matrix-supported beds including detrital residual clays and a mix of carbonate and iron oxides coeval with the karst development (**Figure 3e**). Alternatively, clast-supported sediments present sub-rounded fragments of iron oxides and calcite. These clasts are cemented by secondary massive or drusy calcite (**Figure 3f**). Finally, a synoptic paragenetic sequence can be proposed for all the studied deposits as shown in **Figure 3g**.

3. Methods and sampling

3.1. Sampling strategy

Using a portable gasoline drill, a total of 157 cores has been collected from non-sulphide Zn ore (98 cores), internal sediment (39 cores) and host Lower Jurassic limestone (20 cores) in four localities (**Figure 1b**): Aït Labbès (AL), Toulal (T), Beni Tajite (BT) and Tadaghast (TA). At Aït Labbès, 51 cores (38 of non-sulphide Zn ore, 9 of internal sediment and 4 of host limestone) were sampled in a bunch of N60°-trending cavities at 3 sites (i.e. AL1, AL2 and AL3; **Figures 4a, 4b and 4c**). At the Toulal prospect, 47 cores (15 of non-sulphide Zn ore, 22 of internal sediment and 10 of host limestone) were collected at 3 sites (i.e. T1, T2 and T3; **Figures 4d, 4e and 4f**). At Beni Tajite, 30 cores were drilled in grey non-sulphide Zn ore (i.e. BT1 and BT2; **Figure 4g**). Finally, 29 cores (15 of non-sulphide Zn ore, 8 of internal sediment and 6 of host limestone) were collected at Tadaghast, in the currently exploited galleries with two sites corresponding to E-W sub-vertical and stratabound veins (TA1 and TA2, respectively; **Figures 4h and 4i**). Cores have been oriented with both magnetic and sun compasses, when it was possible, to correct the local magnetic field anomalies. The average difference between magnetic and solar declinations is about 5.8°. In additions, two blocks oriented on field have been collected at Toulal (T3) and Tadaghast (TA6) and further drilled in lab. Then, cores were cut into standard specimens of 22 mm in length and 25 mm in diameter for both AMS and palaeomagnetic measurements.

3.2. Methods and analytical procedure

3.2.1. Anisotropy of Magnetic Susceptibility (AMS)

Magnetic susceptibility (K) is defined by K=M/H where M is the induced magnetization of the material and H, the inducing magnetic field (see Rochette et al. 1992 for details). The susceptibility is described as a symmetric second rank tensor, which can be depicted by an ellipsoid defined by three orthogonally oriented axes: K_1, K_2 and K_3 (with $K_1 \geq K_2 \geq K_3$). K_1 and K_3 are considered to be the magnetic lineation and the pole of the magnetic foliation, respectively. Thus, the Anisotropy of Magnetic Susceptibility (AMS) is the property of a material whereby a given magnetic field applied in different directions produce variable intensities of induced magnetization. A number of parameters can be calculated to characterize the AMS ellipsoid, but the most widely used are the mean magnetic susceptibility (K_m), the corrected anisotropy degree (P_J), and the shape parameter (T) (Tarling and Hrouda 1993). In the case of low susceptibility, these parameters and especially the P_J values should be used with caution, as it has not been corrected from the diamagnetic component (not measured in this study). The AMS is a physical property of rocks that define the magnetic fabric and is used for characterizing internal rock textures and structures (e.g. Hrouda 1982; Sizaret et al. 2003; Charles et al. 2009; 2012; Essalhi et al. 2009).

3.2.2. Palaeomagnetism

Palaeomagnetism relies on the study of the magnetic remanence involved by ferromagnetic *s.l.* minerals present in the rocks. During sediment deposition, or syn-diagenetic precipitation, these minerals may record the Earth magnetic field that can be preserved through time and be used for indirect age constraints (e.g. Van der Voo 1993). Dating ore deposition through palaeomagnetism, especially stratabound, disseminated and massive sulphide ore deposits has beneficiated of major advances since last two decades (e.g. Symons et al. 1996; 2002; Symons and Stratakos 2000; Leach et al. 2001; Bradley and Leach

2003; Pannalal et al. 2008). Palaeomagnetism can be also used to establish the timing of weathering, with characteristic example of laterite profiles or gossans (Théveniaut and Freyssinet 1999; 2002; Théveniaut et al. 2007; Ricordel 2007; Ricordel-Prognon et al. 2010; Essalhi et al. 2011). Hence, the absence of time constraints for non-sulphide Zn-Pb deposits of Moroccan High-Atlas could be overcome using palaeomagnetism coupled with field observations and a detailed mineralogical study (Choulet et al. 2014).

3.2.3. Technical procedure

Prior to carry out the AMS and palaeomagnetic studies, magnetic mineralogy has been investigated by four techniques: (1) X-ray diffraction (INEL XRM3000 diffractometer in transmission mode coupled to an INEL CPS 120 curved position sensitive detector), (2) thermomagnetic measurements (AGICO CS3 coupled with AGICO KLY3-S Kappabridge apparatus), (3) Isothermal Remanent Magnetization (IRM; AGICO JR5-A spinner magnetometer coupled with ASC Scientific IM-10-30) and (4) bulk magnetic susceptibility (AGICO KLY3-S Kappabridge apparatus). We have further measured the Anisotropy of Magnetic Susceptibility using AGICO KLY-3S Kappabridge apparatus and the average orientation of the three principal ellipsoidal axes of AMS for groups of samples was computed with ANISOFT software using Jelinek's statistics (Jelinek 1981). Both thermal and Alternative Field (AF) demagnetizations have been carried out by laboratory-built furnace and AGICO LDA-3 demagnetizer, respectively. Step heating includes an average of ten steps between natural remanent magnetization (NRM) and 680°C. The magnetic remanence was measured using AGICO JR5-A spinner magnetometer to remove recent viscous remanent magnetization components from the magnetic remanence of specimens. The directions of the magnetic remanence were isolated by principal component analysis (Kirchvink 1980) and

mean directions were computed by spherical statistics (Fisher 1953) using palaeomagnetic software packages of Cogné (2003) and R. Enkin (unpublished). All measurements were performed at Institut des Sciences de la Terre d'Orléans (ISTO).

4. Results

4.1. Magnetic mineralogy of non-sulphide Zn-Pb deposits and internal karstic sediment

X-ray diffraction pattern reveals that red ore is composed of goethite, calcite and smithsonite (**Figures 5a and 5b**), whereas grey calamine only includes smithsonite (**Figure 5c**). For internal sediments, goethite, calcite and quartz have been identified (**Figure 5d**), and the large bulge at small θ values attests for a significant clay minerals component. These results are in accordance with field and microscopic observations (**Figures 2 and 3**).

Bulk magnetic susceptibility intervals for each lithology are plotted in **Figure 6**. The majority of ore samples present magnetic susceptibilities lower than 200.10^{-6} SI and up to 800.10^{-6} SI suggesting the contribution of ferromagnetic *s.l.* minerals. The magnetic susceptibilities of internal sediment and host limestone samples are weakly positive (below 100.10^{-6}SI), suggesting that both rock types include paramagnetic minerals, with a small amount of ferromagnetic *s.l.* minerals. In addition, several ore samples (mainly grey ore) display negative values of bulk magnetic susceptibility, suggesting the dominance of diamagnetic minerals, like iron free carbonate.

Isothermal remanent magnetization (IRM) was carried out on 11 representative samples (ores and internal sediments), and results are presented in **Figure 7**. For this technique, samples are magnetized in an increasing direct magnetic field and the resulting IRM saturation pattern is typical of the different ferromagnetic *s.l.* minerals. The red ore and

internal sediments samples from Aït Labbès, Toulal and Tadaghast show similar patterns (**Figures 7a, 7b and 7d**). Samples exhibit a first rapid increase of the induced field at weaker applied fields leading to consider the presence of low-coercive minerals (e.g. magnetite). Then, a lack of magnetic saturation at an applied magnetic field up to 1.4 T is observed, which is typical of high-coercive minerals, such as goethite and/or hematite. For the grey ore of Beni Tajite (**Figure 7c**), the saturation below 150 mT indicates the occurrence of low-coercive minerals (e.g. magnetite). The magnitude of remanence confirms the low concentration of magnetic minerals.

Thermal monitoring of the magnetic remanence and the magnetic susceptibility (Curie temperature evaluation) are presented in **Figure 8**. For the red ore collected at Aït Labbès, Toulal and Tadaghast, thermomagnetic curves (**Figures 8a, 8b and 8c**) present two or three drops of the magnetic remanence at about 100-120°C, 300-350°C (only for samples AL2-3B and T2-11) and 580°C, corresponding to goethite, maghemite (titanomaghemite) and magnetite Curie temperatures, respectively. These observations are partially confirmed by thermal magnetic measurements with magnetic susceptibility dropping at around 300-350°C and 580°C (**Figure 8d)**. The presence of hematite, observed under microscope (Choulet et al. 2014) is probable, as magnetic remanence and susceptibility values continue to slightly drop beyond 580°C (**Figures 8a to 8d**). For internal sediments, the evolution of the magnetic remanence with temperature is the same for each locality, with two drops at around 100-150°C and 580°C (**Figures 8e, 8f and 8g**), in accordance with the presence of goethite and magnetite. Minor hematite is also suspected by the slight drop at 580°C (especially for sample T1-17). This observation partially coincides with thermal magnetic measurements as magnetic susceptibility dropping up to 580°C is due to the magnetite Curie temperature (**Figure 8h**). As for the red ore, hematite is probably present owing to the pattern of magnetic remanence and susceptibility curves above 580°C (**Figure 8f**).

4.2. Magnetic fabric study (AMS)

At Aït Labbès, the AMS pattern is highly heterogeneous for red ore samples, with variable directions of the principal axes and broad error ellipses (**Figure 9a**). Nevertheless, magnetic foliation appears to be relatively steep and roughly parallel to the azimuth of the karst cavity (~N50°). For internal sediments, the magnetic foliation is well-defined and horizontal, with a weakly constrained E-W lineation. In the host limestone, the lineation presents a NW-SE trending and the magnetic foliation is slightly oblique, about 20°, a value close to the dip of the bedding (**Figure 4a**). Both ore and internal sediment samples present low values of the corrected anisotropy degree (P_J<1.01), without correlation with bulk susceptibility, except for high values of susceptibility (**Figure 9a**). The coexistence of positive and negative values of the shape parameter suggests that fabrics are both prolate and oblate. Conversely, in the host limestone, P_J value is higher than 1.01, whilst bulk susceptibility is very low; T value is positive and fabric is apparently oblate.

At Toulal, both ore and internal sediment samples present homogenous measurements of the AMS principal axes directions, with a well-defined horizontal foliation and poorly constrained WNW-ESE lineation (**Figure 9b**). As the host limestone is homogeneous for all three sites, AMS measurements have been compiled into one stereogram (**Figure 9b**). The fabric is quite well-defined and foliation exhibits a strong south-eastward dipping. In ore samples, positive and negative T values are observed, as well as a strong variability of the P_J parameter that is correlated with bulk susceptibility; the higher susceptibility is, the less the corrected anisotropy degree is. Conversely, only oblate fabrics are observed for internal sediments (positive T values), while P_J varies from 1 to 1.06 (**Figure 9b**).

The grey ore samples from Beni Tajite display a well-defined horizontal foliation and NW-SE trending lineation (**Figure 10a**). The majority of T values are positive, suggesting a dominantly oblate shape. Values of the corrected anisotropy degree are bracketed between 1.01 and 1.17, without correlation with bulk susceptibility.

As for Aït Labbès, the ore samples from Tadaghast display heterogeneous AMS pattern, with variable directions of principal axes and large envelope error (**Figure 10b**). Both positive and negative T values are observed, while P_J and bulk susceptibility values are homogeneously weak. For the internal sediments, the fabrics are fairly defined with a horizontal foliation and NW-SE lineation (**Figure 10b**). AMS parameters show P_J values comprised between 1.02 and 1.04 with a bulk magnetic susceptibility yielding from 300 to 900.10^{-6} SI. Finally, the fabrics of the host limestone are quite well-defined with an steeply inclined foliation (up to 70°). The P_J parameter varies from 1.01 to 1.04, while bulk susceptibility (K_m) is very low (i.e. $<10^{-5}$ SI).

4.3. Palaeomagnetic results

The palaeomagnetic study was carried out on samples from Aït Labbès, Toulal and Tadaghast localities. The average measured directions for specimen, sites and localities with the corresponding statistical parameters are reported in **Table 2**.

4.3.1. Aït Labbès deposit

Stepwise demagnetization shows two principal magnetic components for red ore samples distinguished at about 100-150°C (**Figures 11a and 11b**). The low-temperature component (LTC) below 100-150°C is plunging downwards but its direction is scattered, not

consistent with the present-day geomagnetic field. The Characteristic Remanent Magnetization (ChRM) decays to the origin and is, either south to south-southwestwards and plunging upwards (**Figure 11a**) or north to northeastwards and plunging downwards (**Figure 11b**). Although the two opposed polarities are not strictly antipodal, and the reversal test (McFadden and McElhinny 1990) is negative (**Figure 11c**), the average direction of the two groups are similar within errors and a specimen-mean direction for red ore can be calculated at D = 11.1°, I = 42.8°, k = 31, α_{95} = 4.9°, with D and I as the respective declination and inclination of the remanent magnetization, k as the precision parameter and α_{95} as the radius of the 95% confidence circle (**Table 2**). After removing a scattered LTC, internal sediment specimens display a CHRM pointing toward to the origin (**Figure 11d**) with an unblocking temperature over 100-150°C. This component is chiefly north to north-northeastward and plunging upwards (**Figure 11d**). In addition, a south to southeastward and downward component is also observed from two specimens (**Figure 11e**). A specimen-mean direction from internal sediment can be calculated at D = 11.5°, I = 55.0°, k = 12.5, α_{95} = 19.7°, although these two groups with opposed polarities are not strictly antipodal (**Table 2**) and the reversal test is not positive.

4.3.2. Toulal prospect

At Toulal, all samples display a scattered LTC (northwestwards and dipping downwards). Red ore samples present a ChRM decaying to the origin, with unblocking temperatures at 100-150°C. This component is either northward and downward (**Figure 12a**), or south to south-southeastward and upward (**Figure 12b**). Despite a negative reversal test, the two groups of opposed polarities are antipodal, with mean directions similar within errors; a specimen-mean direction at D = 356.0°, I = 47.3°, k = 54.0, α_{95} = 7.1°, has been calculated

for the red ore samples at this locality (**Figure 12c and Table 2**). Identically, a north-northwestward and dipping downward LTC is present in the internal sediments. The ChRM (above 250°C) points to the origin, although demagnetization is not total for several hematite rich specimens. Both northward and downward (**Figure 12d**), or south to south-southwestward and upward (**Figure 12e**) directions have been observed for this component. Despite scattering of individual specimens with reverse polarities, the two groups are antipodal with positive reversal test, and we have calculated a specimen-mean direction at D = 356.7°, I = 34.9°, k = 22.4, α_{95} = 9.4° for internal sediment (**Figure 12f and Table 2**).

4.3.3. Tadaghast deposit

Conversely at Tadaghast, both red ore and internal sediment samples present a characteristic remanence magnetization (ChRM) decaying to the origin, after removing the rare and scattered LTC. For ore specimens, the direction of this ChRM is south-southeastward and plunging upwards (**Figure 13a**). Individual data are scattered (**Figure 13b**) and the calculated specimen-mean at D = 154.4°, I = -57.2°, k = 18.7, α_{95} = 18.2° displays a high statistical variability (**Table 2**). For internal sediment, the direction of ChRM is northeastward and plunging downward (**Figure 13c**). Oppositely, data are grouped and at a specimen-mean has been calculated at D = 20.3°, I = 34.1°, k = 216.1, α_{95} = 4.1° (**Figure 13d and Table 2**).

4.3.4. Beni Tajite deposit

Only 4 specimens out of 10 measured samples have produced a significant remanent magnetization, probably due to a low concentration in ferromagnetic minerals. A ChRM component has been isolated between 300°C and 600°C (**Figure 13e**). As its direction is

relatively scattered and the number of specimen is small (**Figure 13f**), we cannot compute an average paleomagnetic direction and utilize it for dating this deposit.

5. Discussion

5.1. Internal structures of non-sulphide Zn-Pb deposits

Investigation of magnetic carriers has shown that internal sediment and red ore contain soft coercive minerals, magnetite and minor maghemite, and hard coercive minerals, like goethite with minor hematite (**Figure 7 and 8**). In grey ore and host limestone, the dominant magnetic carriers of susceptibility and remanence are often diamagnetic and paramagnetic minerals, although several samples may include a small amount of magnetite (**Figure 7**).

Iron oxi-hydroxides have been observed under optical and electronic microscopes in all deposits. Choulet et al. (2014) have established that both minerals pseudomorph pyrite depending on local pH conditions during early stage of supergene weathering. In addition, goethite may occur later in the succession to form thin bands that alternate with drusy smithsonite (**Figures 3b and 3c**) or to fill voids within geodes (**Figure 3d**). In all cases, goethite and hematite precipitate from iron-saturated solution, implying that the magnetic property, especially the magnetic remanence of the high temperature component partly carried by hematite is of chemical origin. In internal sediments, the iron oxi-hydroxides (hematite and goethite) have formed during diagenesis and thus imply a remanent magnetization of chemical origin too. However, the magnetic remanence is often totally removed at 580°C, so that chemical remanent magnetization is not the dominant one in both types of rocks. Our study of the magnetic mineralogy has also shown the ubiquitous occurrence of magnetite. In sedimentary rocks, magnetite is of detrital origin and its magnetic properties have been

acquired during particle deposition. Magnetite can also be formed during diagenesis and long-lived burial (Aubourg et al. 2012), but such conditions (depth > 2km) have not been reached in karst-related internal sediments as well as in red ore veins. Red ore is characterized by a formation under an oxidizing environment, not compatible with the precipitation of magnetite, especially under supergene conditions. Two hypotheses for the presence of magnetite can be advanced: 1) recycling of detrital magnetite initially within the limestone, but released after host rock dissolution, 2) occurrence of very small cavities of internal sediments including detrital magnetite, which is frequently observed in ore samples (Choulet et al. 2014). These results are partly consistent with the magnetic mineralogy investigated in Sardinian non-sulphide ore deposits (Boni et al. 2005). Goethite and hematite represented the main magnetic carriers and magnetite was not identified, as they did not collect samples related to detrital processes, like karstic internal sediment.

According to AMS measurements, internal sediment samples present a sub-horizontal magnetic foliation (**Figures 9 and 10**). A similar pattern is sometimes observed for ore samples, although a local disturbance is also recorded. The data are more scattered in the host limestone, but data are more distributed along a girdle that became horizontal after bedding correction. This suggests that this pre-tilting magnetic fabric was initially horizontal and could correspond to sedimentary deposition. Whatever the rock type, the magnetic lineation is regularly NW-SE to W-E trending (**Figures 9 and 10**), which is consistent with the orientation of the karstic cavities (**Figure 2**). AMS parameters and, especially, the corrected anisotropy degree are generally low for ore and internal sediment (**Table 1**), suggesting that post-deposition deformation is absent or not penetrative. The broad similarity of AMS patterns between ore and internal sediment implies that same parameters control the development of rock internal fabrics. As magnetic lineation parallels the trend of karst-related cavities and magnetic foliation is horizontal whatever the morphology of the cavity, we

suggest that sedimentary processes within the cavity related to karst fluid dynamics driven by the regular network of first order fractures may control the internal structure of infilling material. In addition, the strong obliquity between horizontal magnetic foliation and the surrounding tectonic markers (faults, limestone bedding) argue for a post 40 Ma deposition of ores and internal sediments, after the main tectonic episode of Atlas (Frizon de Lamotte et al. 2009).

Locally, the individual specimens are scattered for a given site (e.g. AL1, AL2; **Figure 9a**), or define an oblique foliation (**Figure 10b**). This perturbation of the AMS signal may be explained by sedimentary recycling of ore and barren material during karst evolution (e.g. for Aït Labbès). In addition, the Atlas range results from multiple superimposed compressive events (Frizon de Lamotte et al. 2009), and these successive reactivations could explain the oblique fabric exemplified at Tadaghast. Hence it is highly probable that the karstic network has formed progressively throughout the Moroccan High Atlas, in relation with major compression events. Although most observations have revealed horizontal bedding in the cavity, early internal karstic sediment may have undergone polyphased tectonics and, as a consequence, the originally horizontal fabric has been tilted or removed during the recent uplift episodes.

5.2. Age(s) of Moroccan High-Atlas non-sulphide Zn-Pb deposits

At Aït Labbès and Toulal localities, we obtained a well-defined ChRM and chiefly antipodal directions that allow us to calculate mean site directions (**Figures 11 and 12**). The presence of two antipodal polarities for each rock type suggests that remanence is not due to a remagnetization and that our dataset averages the secular variations of the Earth magnetic field. This is also confirmed by our investigation of the magnetic mineralogy that suggests

magnetite and hematite as respective carriers of detrital and chemical remanence, acquired during ore and sediment deposition or during late weathering. Although the primary origin of magnetization cannot be surely assessed, the partial detrital origin for remanence may be underlined by general horizontal bedding observed in the field and the shallow inclination of AMS planar fabric. Although for some samples from Aït Labbès the magnetic fabric is not horiziontal, this does not have significant influence on the scattering of remanent directions.

At Tadaghast, we obtained a well-constrained direction for internal sediment, but the individual measurements for red ore are very scattered (**Figure 13**). For each lithology, a sole polarity has been measured, so that the contemporaneity of ore and internal sediment cannot be ascertained. Given our dataset, it is clearly impossible to advocate a primary chemical or detrital origin of the remanence and the hypothesis of late weathering cannot be ruled out. In addition, specimen-mean directions are not consistent between the two rock types and this can be explained by: 1) false orientation of the specimen, because cores have been drilled at lab from an oriented hand sample and 2) magnetic reworking, as AMS fabrics of red ore (**Figure 10**) are clearly oblique suggesting post-deposition tectonics or recent weathering. Despite a relatively good consistency between Tadaghast internal sediments and other localities, we cannot guarantee the reliability of these data, therefore we have excluded them from further interpretation.

As specimen-mean directions calculated for red ore and internal sediment are compatible for each locality (**Table 2**), we computed a specimen-mean direction including these two lithologies at D = 11.1°, I = 44.8°, k = 24.2, α_{95} = 5.0° for Aït Labbès and at D = 356.4°, I = 40.3°, k = 26.5, α_{95} = 6.3° for Toulal (**Figure 14**). Furthermore, we have calculated two palaeomagnetic poles: λ = 114.4°N, Φ = 78.6°E, dp/dm = 4.0°/6.4° for Aït Labbès (32.38°N, -4.33°E) and λ = 196.7°N, Φ = 79.9°E, dp/dm = 4.2°/6.9° for Toulal (32.30°N, -3.99°E). These two poles are statistically different within error. As several

measured specimens display reverse polarity, the upper age limit for localities corresponds to the last magnetic reversal (Brunhes-Matuyama reversal) at ca. 0.78 Ma (Gradstein et al. 2004). **Figure 15** provides a comparison with the Apparent Polar Wander Path (APWP) of Africa (Besse and Courtillot 2002). The Toulal pole is slightly isolated from the APWP but the ellipse of confidence crosscuts the APWP individual poles at 10 Ma, 20 Ma and 30 Ma. Hence, an age between 30 Ma and 10 Ma can be proposed for Toulal. This is consistent with the horizontal AMS fabric that suggested post-tectonics deposition of red ore and internal sediments after the main Atlas episode at ca. 40 Ma (Frizon de Lamotte et al. 2009). Conversely, the palaeomagnetic pole calculated for Aït Labbès intersects the APWP and the age is statistically between 60 Ma and 10 Ma. However, field observation suggested that red ore and internal sediment do not predate the major compression episode at 40 Ma. Hence the age of Aït Labbès pole is bracketed between 40 Ma and 10 Ma, and in detail, the pole plots closer to the 40 Ma pole of APWP than to the younger one's (**Figure 15**). The apparent diachronism between these two localities is in accordance with the differences in AMS fabrics. The AMS pattern at Toulal shows a well-defined horizontal magnetic foliation and a consistent magnetic lineation whose direction parallels the trend of the karst-related cavity. Conversely, both magnetic foliation and lineation are badly constrained at Aït Labbès, suggesting tectonic and sedimentary perturbations after ore and internal sediment deposition.

Palaeomagnetic data support the post-Atlasic age of supergene weathering inferred from field observation (Choulet et al. 2014), but we could not improve this time interval, similarly to Boni et al. (2003) for Sardinia non-sulphide ore deposits. The large age span of our data can be explained by the limited dataset, although narrow ellipses of confidence for pole attest for the reliability of data. Beyond statistically and sampling bias, the limited movements of Africa during the last tens of million years (Besse and Courtillot 2002) preclude a better constraint for recent episodes when age is based on palaeomagnetism.

5.3. Integration into the Moroccan High-Atlas geodynamic context

This study is the first attempt of dating the non-sulphide zinc deposits in the Moroccan High Atlas. The obtained results are consistent with the timing of ore deposition proposed in Choulet et al. (2014). The following evolution may be proposed:

(1) During Mesozoic (**Figure 16a**), the opening of the Atlantic Ocean and the Tethys led to the reactivation of Variscan deep structures into normal faults that control the formation of a series of horsts and grabens (Laville and Piqué 1991; Piqué 1994). During the Early Jurassic, the formation of carbonate platforms with reef limestone in shallow domains is accompanied by deposition of Zn-Pb sulphide lenses throughout the future High Atlas domain (Mouguina 2004). These deposits are mainly concordant with the bedding of the host rock (Leblanc 1968). As presented in section 2, discontinuous sedimentation has been recorded afterwards, until Tertiary inversion tectonics (Frizon de la Motte et al. 2009).

(2) Between 50 Ma and 35Ma, western Mediterranean domains experienced shortening due to convergence between Europe and Africa (**Figure 16b**). As a consequence, the area has recorded compressive tectonics, leading to the formation of the High Atlas fold-and-thrust belt (Frizon de la Motte et al. 2000; 2009). Reactivation of Liassic normal faults into thrusts has controlled the localisation of narrow anticlines (Teixell et al. 2003), as exemplified at Aït Labbès and Toulal (**Figure 16c**). This compression is not responsible for the present topography but can account for a regional uplift, intense erosion and subsequent exhumation of Zn-Pb sulphide lenses. When the water table has fallen down, dissolution of host limestone may have started, as well as supergene oxidation of the sulphide protore (Choulet et al. 2014). The upright position of the ore lenses has facilitated the downward percolation of the surface water leading to the formation of non-sulphide Zn ore deposits.

Coevally, infilling of karst-related cavities has occurred, either as internal karstic sedimentation or as a precipitation from a Zn-rich solution. Both rock types acquired their fabrics, marked by horizontal foliation and lineation tending to be parallel to the trend of dissolution cavities, controlled by the hydrodynamic regime within the karst. Despite a regional arid climate and relatively quiet tectonics between 35Ma and 5Ma (Maley 1980), short wet episodes (Le Houérou 1997) have contributed to enlargement of karst network and deepening of supergene weathering front.

(3) Since 3Ma, a second major shortening episode has affected northern Africa (**Figure 16d**; Frizon de Lamotte et al. 2000; 2009). Although this episode is widely observed and responsible for the present topography (**Figure 16e**), it seems that its effects on non-sulphide Zn ore deposits of Moroccan High-Atlas has remained limited, as magnetic foliation and sedimentary bedding are mostly preserved as horizontal. Conversely, at Aït Labbès or at Tadaghast, the absence of a well-defined foliation or the oblique pattern of the fabric may indicate that this second compression episode has modified the AMS and remanent magnetisation primary patterns. The widespread reverse polarities constrain the upper limit for oxidation to 0.78 Ma and the last reversal of the Earth magnetic field.

6. Conclusions

This is the first attempt of AMS study within non-sulphide Zn ore deposits. It provides crucial information on internal fabrics within ores and on the first-order geometric connections between ore and internal karstic sediment. Results are consistent with field observation and previous interpretations (Choulet et al. 2014). Hence, the dominantly horizontal magnetic foliation and the direction of magnetic lineation that tends to be parallel to the karstic cavities alignment may attest for a control of fabrics by karst hydrodynamics.

Locally, rock magnetism signal has been removed or fabrics have been tilted due to late superimposed tectonic events.

Palaeomagnetism was successfully applied on both ore and internal karstic sediment from three deposits and obtained results are compatible with age constraints inferred from field observations. Our results support a post-tilting paleomagnetic record that we interpret as of primary origin; it has been acquired either during chemical alteration of ore vein due to rock exhumation or during internal sedimentation processes resulting in the filling of karst-related cavities. Results also suggest local diachronism between deposits, probably due to differences of uplift across the range. However, this last conclusion may be tempered, as our age resolution is not statistically acceptable and we are not able to narrow the time interval between Late Eocene and the last magnetic reversal. The restricted sampling and the limited absolute movement of Africa during the last tens millions years may explain this issue.

As inferred by Boni et al. (2005), this study has shown that palaeomagnetism can be used to constrain the timing of supergene oxidation and the formation of non-sulphide ore deposits. In addition, coupling specimens collected from internal karstic sediment and ore may provide robust results, especially when the rock fabric is controlled by AMS parameters and patterns. Although Sardinian and Moroccan deposits are not ideal cases for high resolution dating, this method may be applied on other examples throughout the world (Belgium, Iran, Vietnam…). In the case of historic deposits of Belgium (Dejonghe 1998), this method could be of great benefit, as field observation only provides a timing of formation between Visean and Cretaceous (Coppola et al. 2008). Besides, the occurrence of supergene willemite mineralisation and its possible use for geochronology (Schneider et al. 2008) may represent a good opportunity to compare both methods and assess the utilisation of palaeomagnetism to timely constrain oxidation episodes.

7. Acknowledgements

This study has benefited from financial support by the Région Centre and Managem in the frame of the 2011-2013 project "Calamines". Many thanks are due to L. El Hassani, O. Baha and M. Maftou Si Med for field support and for providing access to the different mines. Many thanks are due to B Lehmann and A Cheilletz for handling manuscript and to two anonymous reviewers for their constructive comments that greatly improved the manuscript.

8. References

Agard J, du Dresnay R (1965) La région minéralisée du Jbel Bou-Dahar, près de Beni Tajjit (Haut-Atlas oriental) : Étude géologique et métallogénique. Notes et Mém Serv Géol Maroc 181:135-166 (in French).

Auajjar J, Boulègue J (1999) Les minéralisations Pb-Zn-(Cu) Ba du socle paléozoïque et de la plate-forme liasique du district du Tazekka (Taza, Maroc oriental): une synthèse. Chron Rech Min 536-537:121-135 (in French).

Aubourg C, Pozzi J-P, Kars M (2012) Burial, claystones remagnetization and some consequences for magnetostratigraphy. Geol Soc London, Sp Pub 371:181-188.

Bazin D (1968) Etude géologique et métallogénique des chaînons atlasique du Tizi n'Firest au Nord de Ksar-es-Souk, Maroc. Notes et Mém Serv Géol Maroc 206:37-114 (in French).

Besse J, Courtillot V (2002) Apparent and true polar wander and the geometry of the geomagnetic field over the last 200 Myr. J Geophys Res 107:doi:10.1029/2000JB000050.

Boni M, Gilg HA, Aversa G, Balassone G (2003) The “Calamine” of SW Sardinia (Italy): geology, mineralogy and stable isotope geochemistry of a supergene Zn mineralization. Econ Geol 98:731-748.

Boni M, Dinarès-Turell J, Sagnotti L (2005) Paleomagnetic dating of non-sulfide Zn-Pb ores in SW Sardinia (Italy): a first attempt. Ann of Geoph 48:301-312.

Boni M, Terracciano R, Evans N, Laukamp C, Schneider J, Bechstädt T (2007) Genesis of vanadium ores in the Otavi Mountainland (Namibia). Econ Geol 102:441-469.

Boni M, Balassone G, Arseneau V, Schmidt P (2009) The non-sulphide zinc deposit at Accha (Southern Peru): geological and mineralogical characterization. Econ Geol 104:267-289.

Borg G (2003) Surface-related formation, upgrading, and improvement of ore deposits - a review of supergene metallogenic processes. In: Eliopoulos DG et al. (Ed.), Mineral Exploration and Sustainable Development. Millress, 61-64.

Borg G, Kärner K, Buxton M, Armstrong R, van der Merve, Schalk W (2003) Geology of the Skorpion non-sulphide deposit, southern Namibia. Econ Geol 98:749-771.

Borg G (2009) The role of fault structures and deep oxidation in supergene base metal deposits. In: Titley SR (Ed.), Supergene Environments, Processes and Products. Econ Geol Spec Publ 14:121-132.

Bouchaou L (1988) Hydrogéologie du basin des sources karstiques du complexe calcaire Haut-Atlasien du Dir de Beni-Mellal (Maroc). Dissertation, Université de Besançon (in French).

Bradley DC, Leach DL (2003) Tectonic controls of Mississippi Valley-type lead-zinc mineralization in orogenic forelands. Miner Deposita 38:652-667.

Brechbühler YA, Bernasconi R, Schaer JP (1988) Jurassic sediments of the Central High Atlas of Morocco: deposition, burial and erosion history. In: Jacobshagen V (Ed.), The Atlas System of Morocco. Lect Notes Earth Sci 15:139-168.

Bruyère D, De Putter T, Decrée S, Dupuis C, Fuchs Y, Jamoussi F et al (2010) Miocene karsts and associated Fe-Zn-rich minerals in Aïn Khamouda (Central Tunisia). J Afr Earth Sci 57:70-78.

Caïa J (1968) Roches éruptives basiques et minéralisations en plomb, zinc et strontium de la région de Tirrhist (Haute-Atlas de Midelt). Notes et Mém Serv Géol Maroc 206:7-30 (in French).

Charles N, Faure M, Chen Y (2009) The mechanism emplacement of the Montagne Noire migmatitic dome (French Massif Central): New insights from petrofabric and AMS studies. J Struct Geol 31:1423-1440.

Charles N, Gumiaux C, Augier R, Chen Y, Faure M, Lin W, Zhu R (2012) Metamorphic Core Complex dynamics and structural development: Field evidences from the Liaodong Peninsula (East China). Tectonophysics 560-561:22-50.

Charrière A, Haddoumi H, Mojon PO (2005) Découverte de Jurassique supérieur et d'un niveau marin du Barrémien dans les “couches rouges” continentales du Haut-Atlas central marocain : implications paléogéographiques et structurales. C R Palevol 4:385-394 (in French).

Charrière A, Haddoumi H, Mojon PO, Ferrière J, Cuche D, Zili L (2009) Mise en évidence par charophytes et ostracodes de l'âge paléocène des dépôts discordants sur les rides anticlinales de la région d'Imilchil (Haut-Atlas, Maroc): conséquences paléogéographiques et structurales. C R Palevol 8:9-19 (in French).

Chèvremont P (1975) Les roches éruptives basiques des boutonnières de Tassent et Tasraft et leurs indices métallifères dans leur cadre géologique (Haut-Atlas central, Maroc). Dissertation, Université Claude-Bernard, Lyon (in French).

Choulet F, Charles N, Barbanson L, Branquet Y, Sizaret S, Ennaciri A, Badra L, Chen Y (2014) Non-sulfide zinc deposits of the Moroccan High Atlas: Multi-scale characterization and origin. Ore Geol Rev 56:115-140.

Cogné JP (2003) PaleoMac: a Macintosh™ application for treating paleomagnetic data and making plate reconstructions. Geochem Geophys Geosyst 4(1):1007.doi:10.1029/2001GC000227.

Cole PM, Sole KC (2002) Solvent extraction in the primary and secondary processing of zinc. J South Afr Inst Min Metall 102:451-456.

Coppola V, Boni M, Gilg HA, Balassone G, Dejonghe L (2008) The “calamine” nonsulfides Zn-Pb deposits of Belgium: petrographical, mineralogical and geochemical characterization. Ore Geol Rev 33:187-210.

Couvreur G (1978) Le rôle de la lithologie dans l'évolution des formes karstiques majeures du Haut Atlas central calcaire (Maroc). Rev Geogr Phys 66:309-311 (in French).

Daliran F, Borg G, Armstrong R, Walther J, Vennemann T, Friese K et al (2009) Non sulphide zinc deposits, Iran - the hypogene emplacement and supergene modification history of the Angouran Zinc Deposit, NW-Iran. Berichte zur Lagerstätten und Rohstoffforschung, 57. Bundesanstalt für Geowissenschaften und Rohstoffe, Hannover, 75 p.

Daliran F, Pride K, Walther J, Berner ZA, Bakker RJ (2013) The Angouran Zn-(Pb) deposit, NW Iran: Evidence for a two stage, hypogene zinc sulphide-zinc carbonate mineralization. Ore Geol Rev 53:373-402.

Decrée S, Marignac C, De Putter T, Deloule E, Liégeois JP, Demaiffe D (2008) Pb-Zn mineralizations in a Miocene regional extensional context: the case of the Sidi Driss and the Douahria ore deposits (Nefza mining district, N. Tunisia). Ore Geol Rev 34:285-303.

Decrée S, Ruffet G, De Putter T, Baele JM, Recourt P, Jamoussi et al (2010) Mn oxides as efficient traps for metal pollutants in a polyphase low-temperature Pliocene environment: a case study in the Tamra iron mine, Nefza mining district, Tunisia. J Afr Earth Sci 57:249-261.

Dejonghe L (1998) Zinc-lead deposits of Belgium. Ore Geol Rev 12:329-354.

du Dresnay R (1979) Sédiments jurassiques du domaine des chaînes atlasiques du Maroc. Symposium “Sédimentation jurassique ouest-européenne”, ASF Publ Spéc 345-365 (in French).

du Dresnay R (1988) Recent data on the geology of the Middle Atlas (Morocco). In: Jacobshagen V (Ed.), The Atlas System of Morocco. Lect Notes Earth Sci 15:293-320.

Emberger A (1965) Carte polygénétique des minéralisations plombifères de la Haute Moulouya (gisements d'Aouli, Mibladen et Zaida), Maroc. C R Acad Sci Paris 260:3433-3436 (in French).

Emberger A (1969) Carte des minéralisations plombo-zincifères du Maroc : gîtes et indices renfermant du plomb ou du zinc en élément majeur ou mineur. Notes et Mém Serv Géol Maroc 215 (in French).

Essalhi M, Sizaret S, Barbanson L, Chen Y, Branquet Y, Panis D, Camps P, Rochette P, Canals A (2009) Track of fluid paleocirculation in dolomite host rock at regional scale by the Anisotropy of Magnetic Susceptibility (AMS): An example from Aptian carbonates of La Florida, Northern Spain. Earth Planet Sci Lett 277:501-513.

Essalhi M, Sizaret S, Barbanson L, Chen Y, Lagroix F, Demory F, Nieto JM, Sáez R, Capitán A (2011) A case study of the internal structures of gossans and weathering processes in the Iberian Pyrite Belt using magnetic fabrics and paleomagnetic dating. Mineral Deposita. doi.10.1007/s00126-011-0361-8.

Fisher RA (1953) Dispersion of a sphere. Proc Roy Soc Lond A217, 295-305.

Frizon de Lamotte D, Zizi M, Missenard Y, Hafid M, El Azzouzi M, Charrière A et al (2008) The Atlas system. In: Michard A, Saddiqi O, Chalouan A, Frizon de Lamotte D (Eds.), Continental Evolution: The Geology of Morocco. Structure, Stratigraphy, and Tectonics of the Africa-Atlantic-Mediterranean Triple Junction. Springer-Verlag 133-202.

Frizon de Lamotte D, Leturmy P, Missenard Y, Khomsi S, Ruiz G, Saddiqi O et al (2009) Mesozoic and Cenozoic vertical movements in the Atlas system (Algeria, Morocco, Tunisia): an overview. Tectonophysics 475:9-28.

Gnoinski J (2007) Skorpion zinc: optimization and innovation. J South Afr Instrum Min Metall 107:657-662.

Gomez F, Allmendinger R, Barazangi M, Beauchamp W (2000) Role of the Atlas Mountains (northwest Africa) within the African-Eurasian plate-boundary zone. Geology 28:775-778.

Gradstein F, Ogg J, Smith A (2004) A geological time scale. Cambridge University Press, 600 p.

Groves I, Carman CE, Dunlap WJ (2003) Geology of the Beltana willemite deposit, Flinders Ranges, South Australia. Econ Geol 98:797-818.

Haddoumi H, Charrière A, Andreu B, Mojon PO (2008) Les dépôts continentaux du Jurassique moyen au Crétacé inférieur dans le Haut-Atlas oriental (Maroc) : Paléoenvironnements successifs et signification paléogéographique. Carnets de Géologie - Notebooks on Geology, Brest. (2008/XX (CG2008 AXX). http://paleopolis.rediris.es/cg/French).

Herbig HG, Trappe J (1994) Stratigraphy of the Subatlas Group (Maastrichtian-Middle Eocene, Morocco). Newsl Stratigr 30:125-165.

Heyl AV, Bozion CN (1962) Oxidized zinc deposits of the United States, part 1. General geology. US Geol Surv Bull 1135-A, 52 p.

Hitzman MW, Reynolds NA, Sangster DF, Allen CR, Carman CE (2003) Classification, genesis, and exploration guides for non sulfide zinc deposits. Econ Geol 98:685-714.

Hosseini SH (2008) Physicochemical Studies of Oxide Zinc Mineral Flotation. Dissertation, University of Technology, Luleå.

Hrouda F (1982) Magnetic anisotropy of rocks and its application in geology and geophysics. Geophys Surv 5:37-82.

Jelinek V (1981) Characterization of the magnetic fabric of rocks. Tectonophysics 79:63-67.

Jemmali N, Souissi F, Vennemann TWM, Carranza EJ (2011) Genesis of the Jurassic carbonate-hosted Pb-Zn deposits of Jebel Ressas (North-Eastern Tunisia): Evidence from mineralogy, petrography and trace metal contents and isotope (O, C, S, Pb) geochemistry. Res Geol 61:367-383.

Kirschvink J (1980) The least squares line and the analysis of palaeomagnetic data. Geophys J R Astron Soc 62:699-718.

Large D (2001) The geology of non-sulphide zinc deposits - an overview. Erzmetall 54:264-276.

Laville E, Piqué A (1991) La distension crustale atlantique et atlasique au Maroc au début du Mésozoïque: le rejeu des structures hercyniennes. Bull Soc Géol Fr 162:1161-1171.

Laville E, Piqué A (1992) Jurassic penetrative deformation and Cenozoic uplift in the central High Atlas (Morocco): a tectonic model. Structural and orogenic inversions. Geol Rundsch 81:157-170.

Laville E, Piqué A, Amrhar M, Charroud M (2004) A restatement of the Mesozoic Atlasic rifting (Morocco). J Afr Earth Sci 38:145-153.

Leach DL, Bradley D, Lewchuk MT, Symons DTA., de Marsily G, Brannon J (2001) Mississipi Valley-type lead-zinc deposits through geological time: Implications from recent age dating research. Mineral Deposita 36:711-740.

Leblanc M (1968) Etude géologique et métallogénique du Jbel Bou Arhous et de son prolongement oriental (Haut-Atlas marocain oriental). Notes Mém Serv Géol Maroc 206:117-206 (in French).

Le Houérou HN (1997) Climate, flora and fauna changes in the Sahara over the past 500 million years. J Arid Env 37:619-647.

Maley J (1980) Les changements climatiques de la fin du Tertiaire en Afrique: leurs conséquences sur l'apparition du Sahara et de sa végétation. In: Williams AJ, Faure H (Eds), The Sahara and the Nile. Balkema, Rotterdam, 63-86.

Mattauer M, Tapponnier P, Proust F (1977) Sur les mécanismes de formation des chaînes intracontinentales. L'exemple des chaînes atlasiques du Maroc. Bull Soc Géol Fr 19:521-526.

McFadden PL McElhinny MW (1990) Classification of the reversal test in palaeomagnetism. Geophys J Int 103: 725-729.

Mouguina EM (2004) Les minéralisations polymétalliques (Zn-Pb, Cu, Co, Ni) du Jurassique du Haut Atlas central (Maroc): Contexte géodynamique, typologies et modèles génétiques. Dissertation, Faculté des Sciences Semlalia, Marrakech.

Nicod J (1997) Karsts et fonctionnement hydrologique dans le Haut Atlas central calcaire et sur la bordure du Moyen Atlas méridional. Ann Geogr 106 :536-538 (in French).

Ovtracht A (1978) Province plombo-zincifère du Haut Atlas central. Mines Géol Energie 44:103-109.

Pannalal SJ, Symons DTA, Sangster DF (2008) Paleomagnetic Evidence for an Early Permian Age of the Lisheen Zn-Pb Deposit, Ireland. Econ Geol 103:1641-1655.

Piqué A, Michard A (1989) Moroccan Hercynides: a synopsis. The Paleozoic sedimentary and tectonic evolution at the northern margin of West Africa. Am J Sci 289:286-330.

Piqué A (1994) Géologie du Maroc, les domaines régionaux et leur évolution structurale. Pumag, Marrakech.

Popov A (1968) Les types morphologiques et la répartition des gisements de zinc et de plomb en Algérie. Ann Min Géol 23:103-203.

Reichert J, Borg G (2008) Numerical simulation and a geochemical model of supergene carbonate-hosted non-sulphide zinc deposits. Ore Geol Rev 33:134-151.

Ricordel C (2007) Datations par paléomagnétisme des paléoaltérations du Massif central et de ses bordures: Implications géodynamiques. Dissertation, Ecole des Mines de Paris.

Ricordel-Prognon C, Lagroix F, Moreau MG, Thiry M (2010) Lateritic paleoweathering profiles in French Massif Central: Paleomagnetic datings. J Geophys Res 115, doi:10.1029/2010JB007419.

Rochette P, Jackson M, Aubourg C (1992) Rock magnetism and the interpretation of the anisotropy of magnetic susceptibility. Rev Geophys 30:209-226.

Rouvier H, Perthuisot V, Mansouri A (1985) Pb-Zn deposits and salt-bearing diapirs in Southern Europe and North Africa. Econ Geol 80:666-687.

Santoro L, Boni M, Herrington R, Clegg A (2013) The Hakkari nonsulfide Zn–Pb deposit in the context of other non sulfide Zn-Pb deposits in the Tethyan Metallogenetic Belt of Turkey. Ore Geol Rev. doi.org/10.1016/j.oregeorev.2013.01.011.

Schneider J, Boni M, Laukamp C, Bechstädt T, Petzel V (2008) Willemite (Zn_2SiO_4) as a possible Rb-Sr geochronometer for dating nonsulfide Zn-Pb mineralization: Examples from the Otavi Mountainland (Namibia). Ore Geol Rev 33:152-167.

Sizaret S, Chen Y, Chauvet A, Marcoux E, Touray JC (2003) Magnetic fabrics and fluid flow directions in hydrothermal systems. A case study in the Chaillac Ba-F-Fe deposit (France). Earth Plan Sci Lett 206:555-570.

Symons DTA, Sangster DF, Leach DL (1996) Paleomagnetic dating of Mississippi Valley-type Pb-Zn-Ba deposits. Soc Econ Geol Spec Vol 4:515-526.

Symons DTA, Stratakos KK (2000) Palaeomagnetic dating of dolomitization and Mississippi Valley-type zinc mineralization in the Mascot-Jefferson city district of Eastern Tennessee: a preliminary analysis. In: Pueyo JJ, Cardellach E, Bitzer K, Taberner C (Ed), Geofluids III, 3rd International Conference on Fluid Evolution, Migration and Interaction in Sedimentary Basins and Orogenic Belts. J Geochem Explor 69-70:373-376.

Symons DTA, Smethurst MT, Ashton JH (2002). Paleomagnetism of the Navan Zn-Pb Deposit, Ireland. Econ Geol 97:997-1012.

Tarling DH, Hrouda F (1993) The magnetic anisotropy of rocks. Chapman and Hall, London.

Terracciano R (2008) Willemite mineralization in Namibia and Zambia. Dissertation, University of Napoli.

Théveniaut H, Freyssinet P (1999) Paleomagnetism applied to lateritic profiles to assess saprolite and duricrust formation processes: The example of the Mont Baduel profile (French Guiana). Palaeogeogr Palaeoclimatol Palaeoecol 148:209-231.

Théveniaut H, Freyssinet P (2002) Timing of lateritization on the Guiana Shield: Synthesis of paleomagnetic results from French Guiana and Suriname. Palaeogeogr Palaeoclimatol Palaeoecol 178:91-117.

Théveniaut H, Quesnel F, Wyns R, Hugues G (2007) Paleomagnetism dating of the “Borne de Fer” ferricrete (NE France): Lower Cretaceous continental weathering. Palaeogeogr Palaeoclimatol Palaeoecol 253:271-279.

Van der Voo R (1993) Paleomagnetism of the Atlantic, Tethys and Iapetus Oceans. Cambridge University Press, New York, 411 p.

Withney DL, Evans B (2010) Abbreviations for names of rock-forming minerals. Am Miner 95:185-187.

Zijderveld JDA (1967) A.C. demagnetization of rocks: Analysis of results. Methods in Paleomagnetism Conference, Amsterdam, Proceedings 254-286.

Figure captions

Figure 1: (a) Simplified tectonic map of western Mediterranean Sea and western North Africa, illustrating the relationships between High Atlas and the Alpine Belt (modified from Gomez et al. 2000). MA: Middle Atlas. (b) Geological map of the Moroccan High Atlas. The location of the Pb-Zn prospects (white circle) and studied ore deposits (yellow star) is also indicated. (c) Cross-section of the Moroccan High Atlas, illustrating the structure of the fold-and-thrust belt and the connection between the Mesozoic cover and the Palaeozoic basement (modified after Teixell et al. 2003).

Figure 2: (a) Panoramic view showing the typical fold-and-thrust structure of the Moroccan High-Atlas with tight and faulted anticline (Aït Labbès ore deposit). (b) View of a karstic cavity, parallel to the N80°E anticline structure, and filled by red calamine during ore extraction (Aït Labbès ore deposit). (c) Aspect of the calamine network, forming N70°E-striking boudin-like veins (Toulal prospect). (d) View of the cavities, previously filled by red ore (Toulal prospect). (e) View of a profile showing stratabound mineralisation, with distribution of Zn-Pb sulphides minerals (bottom) and Zn-Pb non-sulphides minerals (top) (Tadaghast ore deposit). (f) Relation between tilted limestone strata and horizontal marl of internal sediments filling a karstic cavity whose limit is indicated by red dashed line (Toulal prospect). (g) Sample of Zn sulphides and non-sulphides minerals (sphalerite ZnS, smithsonite $ZnCO_3$, Fe-oxides, and hemimorphite $Zn_4Si_2O_7(OH)_2 \cdot (H_2O)$) from Toulal. (h) Red ore sample made of smithsonite and Fe-oxides from Aït Labbès ore deposit. (i) Grey ore sample made of smithsonite, hemimorphite and hydrozincite ($Zn_5(CO_3)_2(OH)_6$) from Beni Tajite ore deposit. Abbreviations for minerals according to Whitney and Evans (2010): Gn: galena, Hmp: hemimorphite, Hyd: hydrozincite, Sp: sphalerite.

Figure 3: Microphotographs of non-sulphide Zn-Pb ores (a to d) and karst internal sediments (e and f) from studied ore deposits. (a) Relics of sphalerite and pyrite (protore) associated with translucent smithsonite. (TL, nic. //). (b) Iron oxi-hydroxides (goethite and hematite) encrusting oxidized smithsonite, both constituting the "red calamine" (RL, nic. //). (c) Alteration stage II smithsonite ("grey ore") growing on primary oxidized stage I smithsonite and postdating the formation of iron oxi-hydroxides. The final filling is made of hemimorphite and calcite (RL, nic. +). (d) "Grey ore" with alteration stage II smithsonite encrusting alteration stage I smithsonite and iron oxides (TL, nic. //). Zoom box: concentric shells of goethite rhythmically encrusting translucent smithsonite (TL, nic. +). (e) Internal sediments: banded Fe-oxides (hematite and goethite) encrusting banded calcite. Others micro-beds are made of smithsonite and Fe-oxides clasts. Note the presence of a smithsonite clast. (TL, nic. +). (f) Zoom on a clastic micro-bed within internal sediments. Clasts of Fe-oxides are cemented by calcite (TL, nic. //). (g) Synoptic paragenetic sequence of observed minerals in studied ore deposits. Vertical lines represent the separation between the protore mineralisation (sulphides) and the two supergene stages (i.e. red-ore and grey-ore). Vertical dashed line corresponds to the limit between the "red ore" and the "grey ore" (modified after Choulet et al. 2014). Mineral abbreviations according to Whitney and Evans (2010): Cal: calcite, Gth: goethite, Hem: hematite, Hmp: hemimorphite, Py: pyrite, Qz: quartz, Sm: smithsonite, Sp: sphalerite. RL: reflected light, TL: transmitted light, nic. //: plane polarized light, nic. +: crossed polarized light.

Figure 4: AMS and palaeomagnetic sampling sites. (a to d) Aït Labbès ore deposit sampling sites. In the sampled zone, the dip of the limestone is about 20° to the NW. (e and f) Toulal prospect sampling sites. (g) Beni Tajite ore deposit with localisation of sampling sites within

galleries. (h and i) Tadaghast ore deposit sampling sites into mineralised E-W vein (h) and horizon (i).

Figure 5: X-ray diffraction patterns of rock powders from Aït Labbès (a), Toulal (b), Beni Tajite (c) and Tadaghast (d) ore deposits. Intensities (y axis) are normalised to the value of the highest peak.

Figure 6: Histogram of bulk magnetic susceptibility (K_m) of all measured samples.

Figure 7: Results of Isothermal Remanent Magnetization (IRM) measurements.

Figure 8: Results of magnetic remanence measurements (a to c and e to g) and thermomagnetic Curie temperature analyses (d and h) for samples of red calamine and internal sediments from Aït Labbès, Toulal and Tadaghast. Abbreviations: HC: heating component, CC: cooling component.

Figure 9: AMS results from Aït Labbès deposit (a) and Toulal prospect (b) for non-sulphide Zn ore, internal sediments and host-rock. Results are represented by equal-area projection of each site. Squares, triangles and circles stand for K_1 (magnetic lineation), K_2 (intermediate axis) and K_3 (pole of magnetic foliation), respectively. Small grey dots and larger black ones represent individual specimen and site-mean direction, respectively. Confidence ellipses at 95% level are drawn for each site-mean direction. AMS scalar parameters are represented by graphs: T (shape parameter) *vs.* P_J (corrected anisotropy parameter), T *vs.* K_m (mean bulk magnetic susceptibility) and P_J *vs.* K_m. Calculations of T and P_J can be found in Jelinek

(1981). Red line indicates the karst cavity azimuth (~N50° for Aït Labbès and ~N80° for Toulal).

Figure 10: AMS results for Beni Tajite deposit (a) and Tadaghast deposit (b). See Figure 9 for details.

Figure 11: Palaeomagnetic results for the Aït Labbès deposit. Orthogonal projections of sample demagnetization (Zijderveld 1967) show reverse (a) or normal (b) polarity for red ore (a) and reverse or normal (d) polarity for internal sediments. Equal-area projections show red ore (c) and internal sediments (e) specimen directions (grey dots) with locality-mean direction (black star), isolated from high temperature or high coercive AF components. Black diamond indicates the position of present-day earth magnetic field.

Figure 12: Palaeomagnetic results for the Toulal prospect. Orthogonal projections of sample demagnetization (Zijderveld 1967) show normal (a) or reverse (b) polarity for red ore and normal (d) and reverse (e) polarity for internal sediments. Equal-area projections show red ore (c) and internal sediments (f) specimen directions (grey dots) with locality-mean direction (black star), isolated from high temperature or high coercive AF components. Black diamond indicates the position of present-day earth magnetic field.

Figure 13: Palaeomagnetic results for the Tadaghast deposit (a to d) and Beni Tajite (e and f). Orthogonal projections of sample demagnetization (Zijderveld 1967) showing reverse polarity for red ore (a) and normal polarity for internal sediments (c). Equal-area projections show red ore (b) and internal sediments (d) specimen directions (grey dots) with locality-mean direction (black star), isolated from high temperature or high coercive AF components. Orthogonal

projections of sample demagnetization for Beni Tajite grey ore (e). Equal-area projections of Beni Tajite grey ore shows scattering of data (f). Black diamond indicates the position of present-day earth magnetic field.

Figure 14: Equal-area projection of specimen remanence directions for both red ore (circles) and internal sediment (triangles) for Aït Labbès (a) and Toulal (b). Stars represent the locality-mean direction.

Figure 15: Palaeomagnetic poles calculated for Aït Labbès and Toulal compared to the APWP of Africa between 100 and 10 Ma (Besse and Courtillot 2002). It appears Aït Labbès and Toulal ore deposits are diachronic.

Figure 16: Tectonic sketches illustrating the development of the non-sulphide Zn-Pb deposits during the evolution of the Moroccan High Atlas with the western Mediterranean area (modified from Choulet et al. 2014, Jolivet et al. 2000; Frizon de Lamotte et al. 2000; 2009). (a) The opening of Atlantic Ocean and Tethys is accommodated by normal faulting. This period corresponds to deposition of reef and para-reef limestones and formation of sulphide lenses. (b and c) During Eocene, normal faults were reactivated as thrusts that accommodate the formation of tight anticlines, related to the High-Atlas intra-continental belt. (d and e) Atlasic main folding stage has involved a verticalization of the stratabound lenses of sulphides and has been followed by successive uplift periods, until Present, which have facilitated the percolation of meteoritic water, the karst formation (deposition of internal sediment) and the coeval to subsequent replacement of sulphide ores by non-sulphides ores.

Table 1: AMS results from red and white ores, internal sediments and host limestone. n: number of specimen taken into statistic calculation; N: number of measured specimen. D, I, α_{95min}, α_{95max} are declination, inclination, Jelinek's statistic confidence at 95% level (Jelinek 1981) in degrees, respectively. P_J: Corrected anisotropy degree, T: Anisotropy shape parameter (Jelinek 1981), and K_m: Mean magnetic susceptibility.

Table 2: Palaeomagnetic results from red ore and internal sediments samples collected in the Moroccan High Atlas. n is the number of steps used in Kirschvink's principal component analysis (PCA), N is the number of specimens used for calculation specimen-mean direction, D and I are the respective declination and inclination of the remanent magnetization, MAD is the main angle deviation obtained from PCA, k is the precision parameter and α_{95} is the radius of the 95% confidence circle.

Figure 1

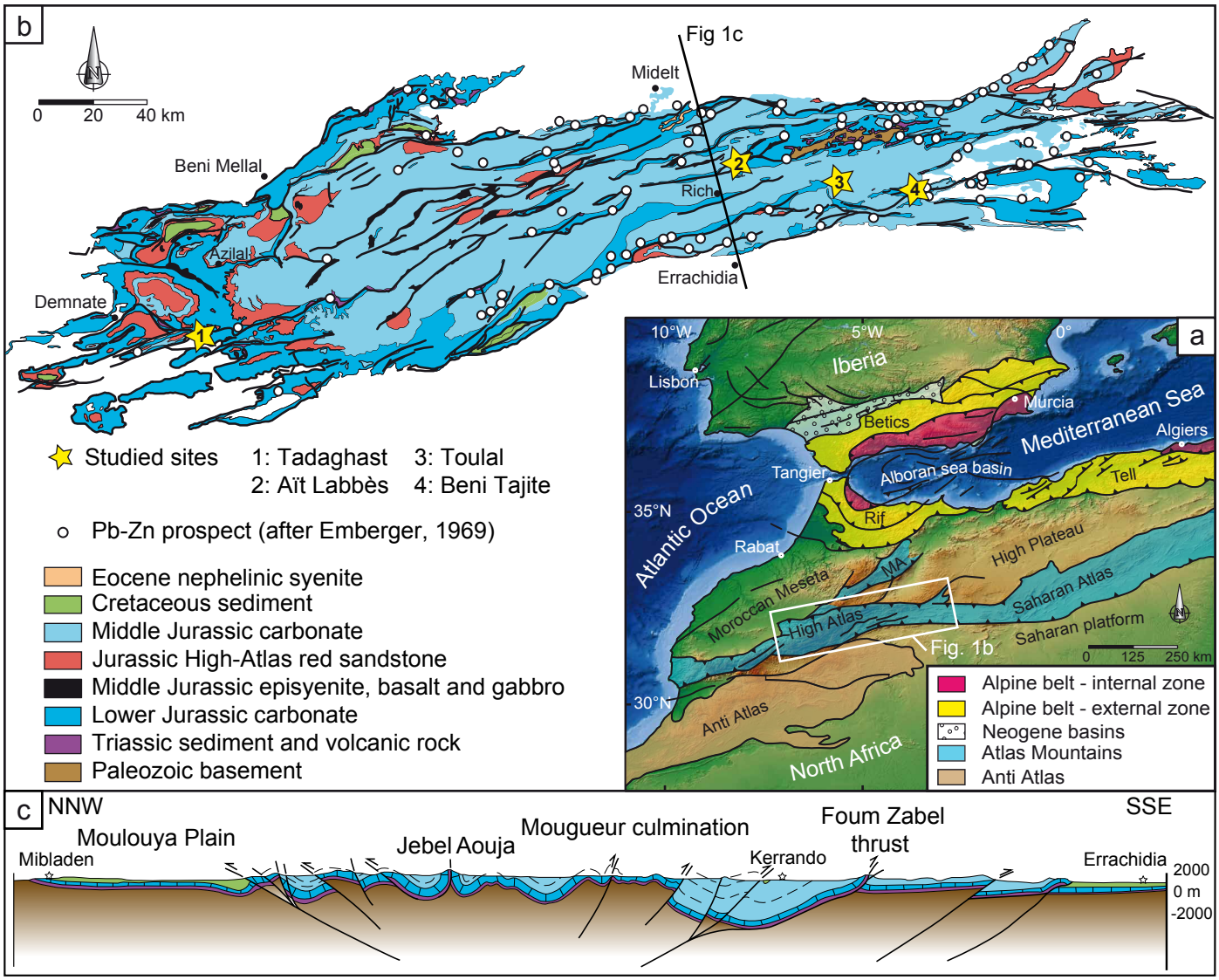

Figure 1

Figure 2

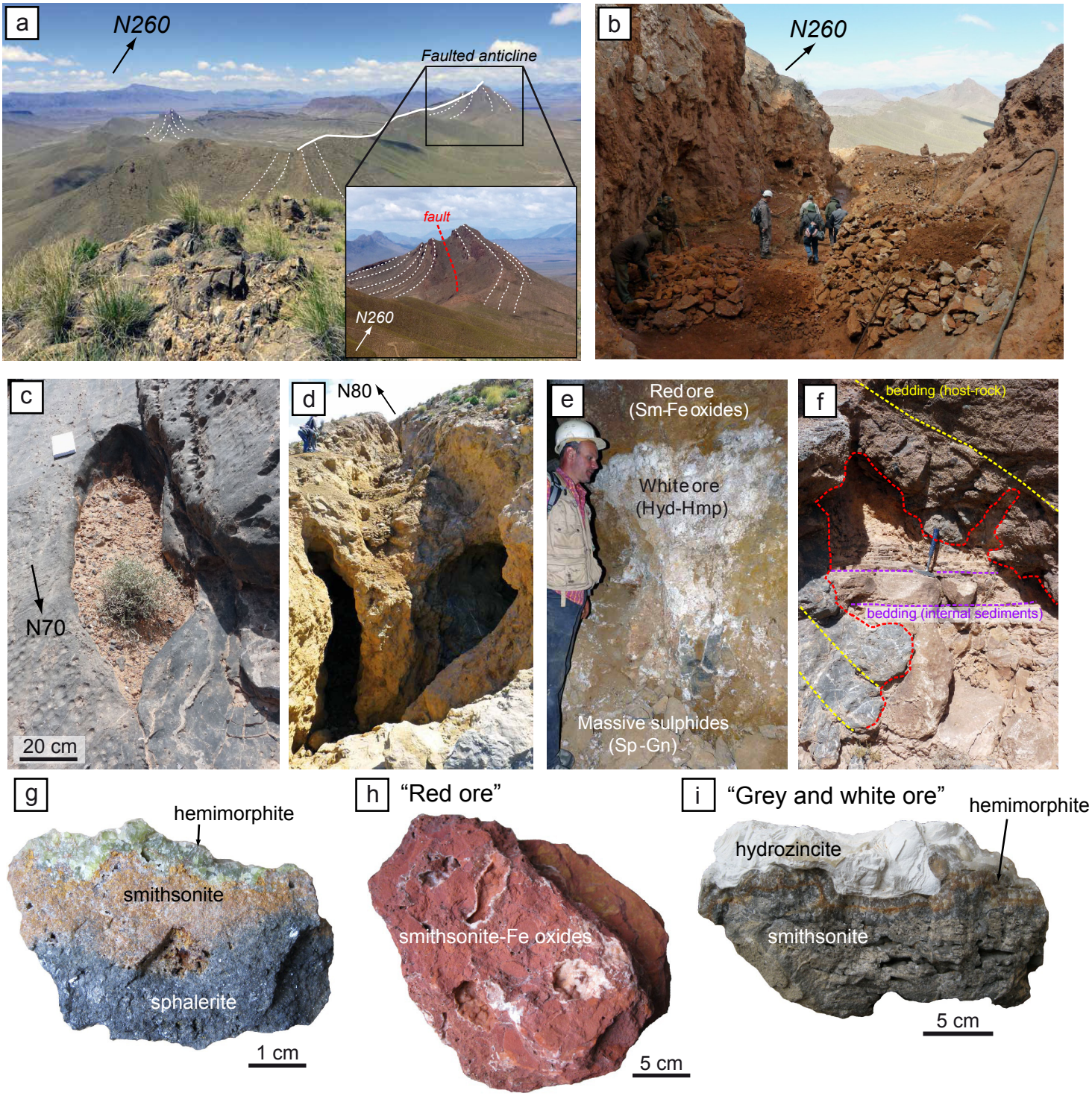

Figure 2

Figure 3

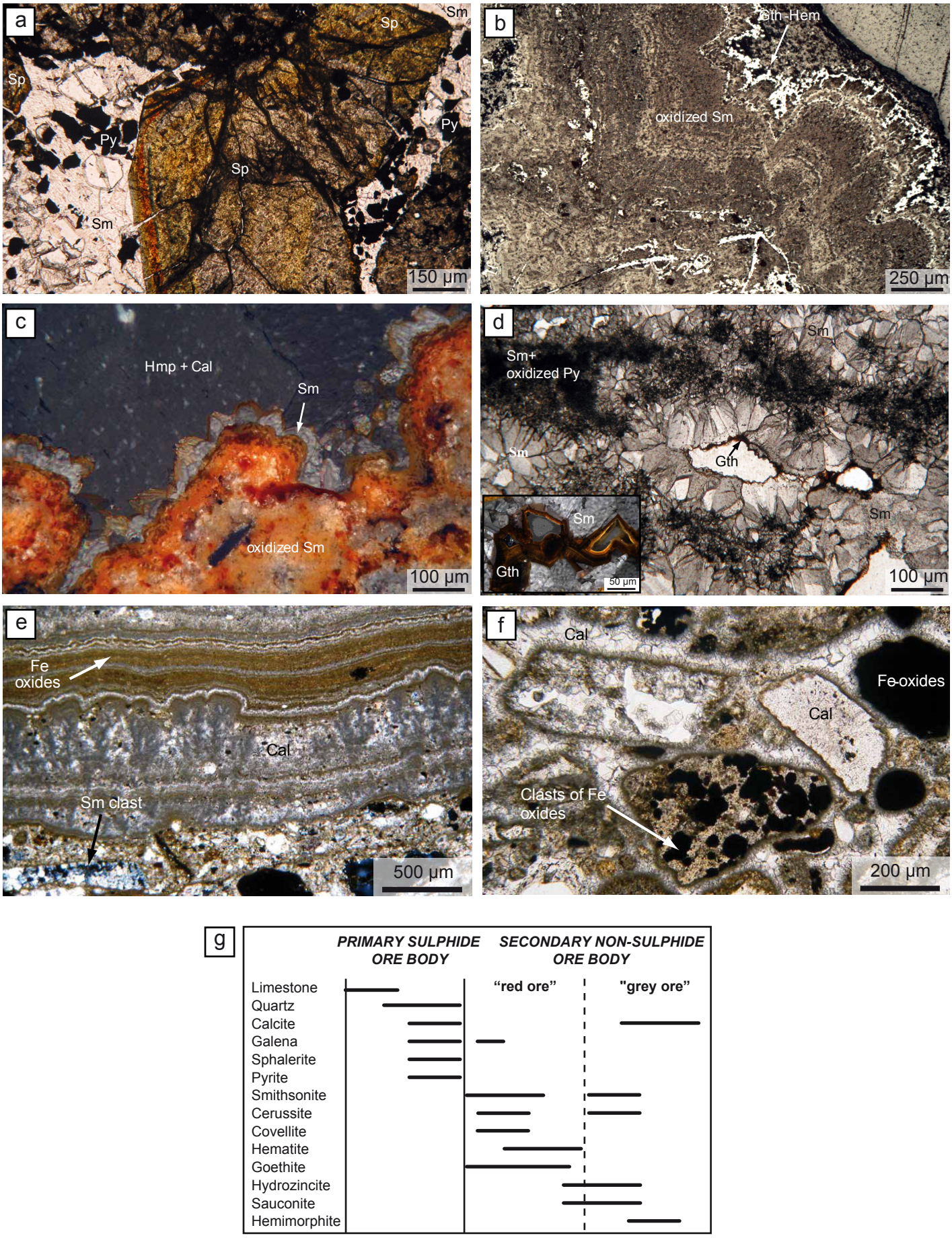

Figure 3

Figure 4

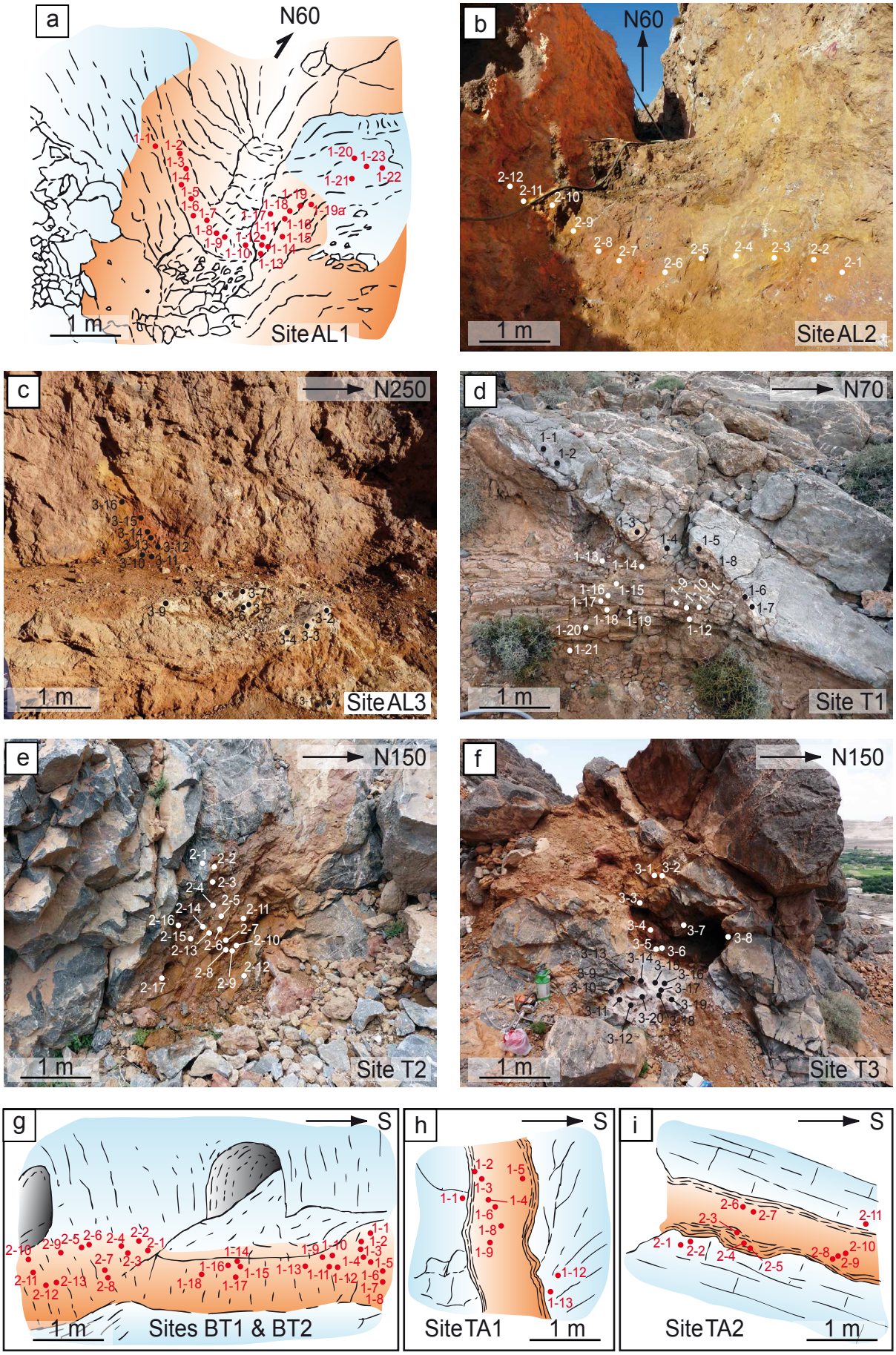

Figure 4

Figure 5

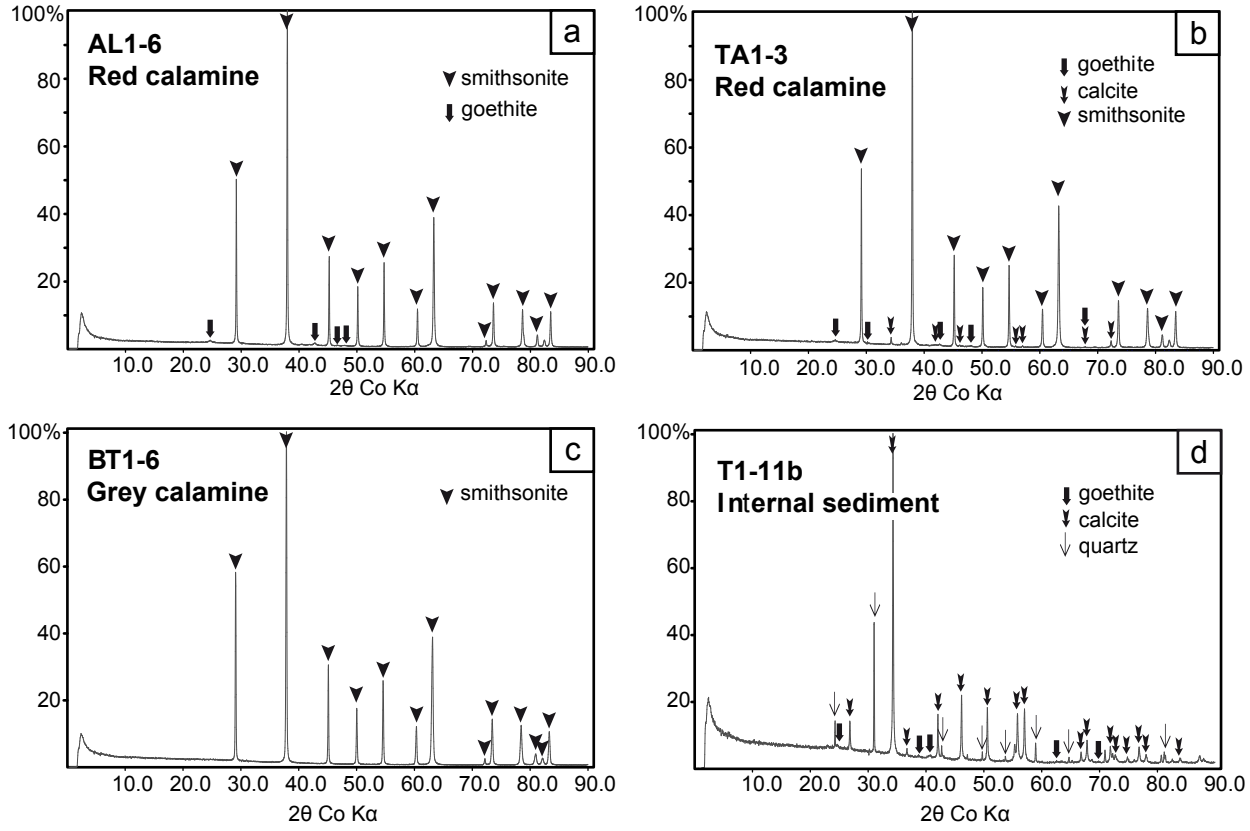

Figure 5

Figure 6

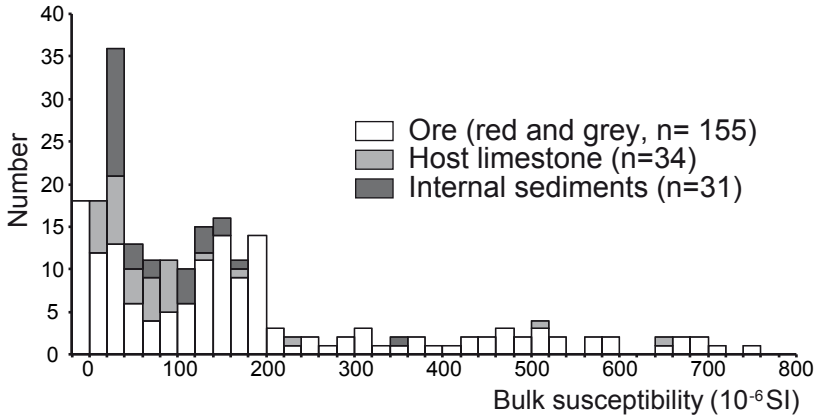

Figure 6

Figure 7

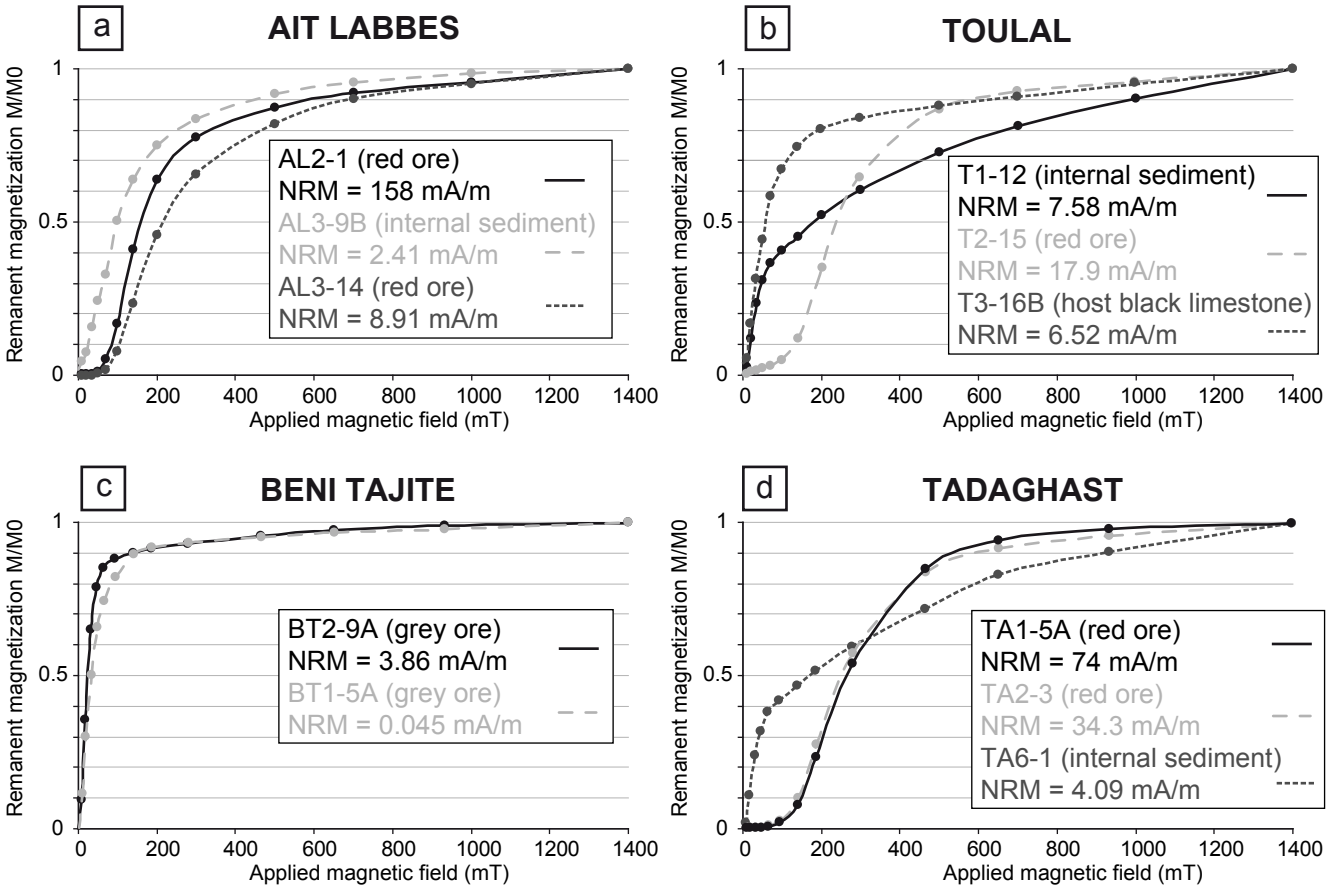

Figure 7

Figure 8

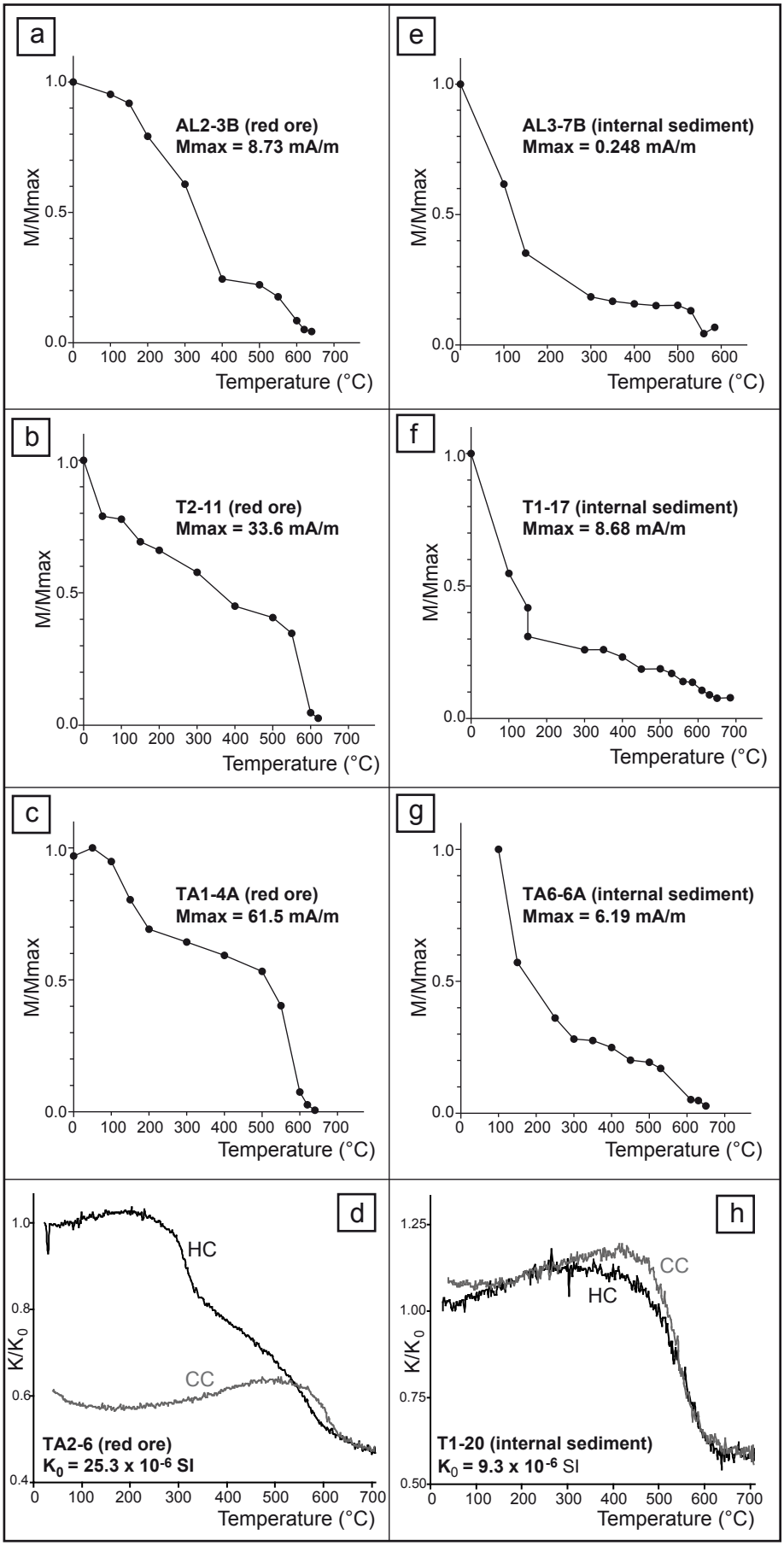

Figure 8

Figure 9

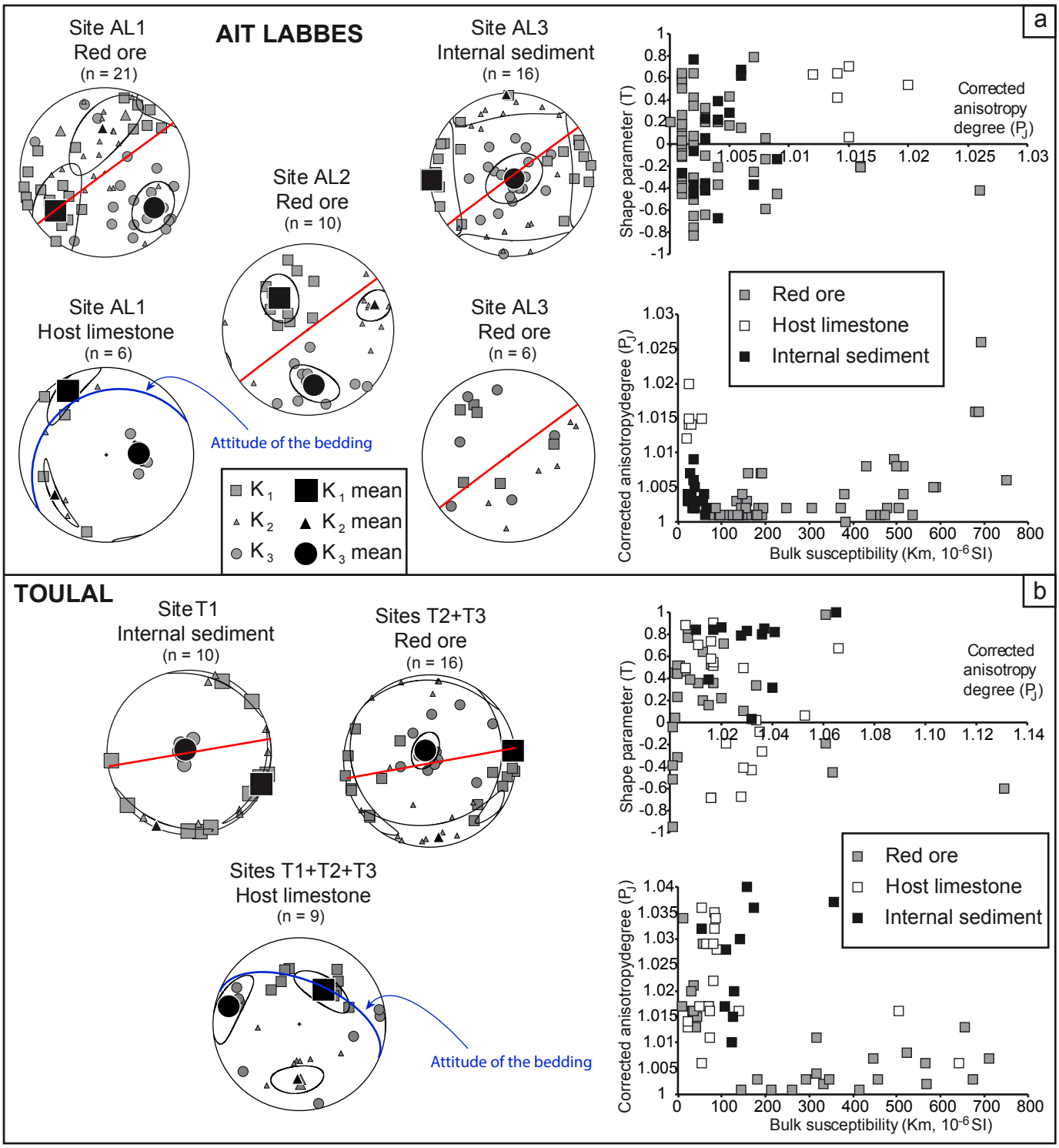

Figure 9

Figure 10

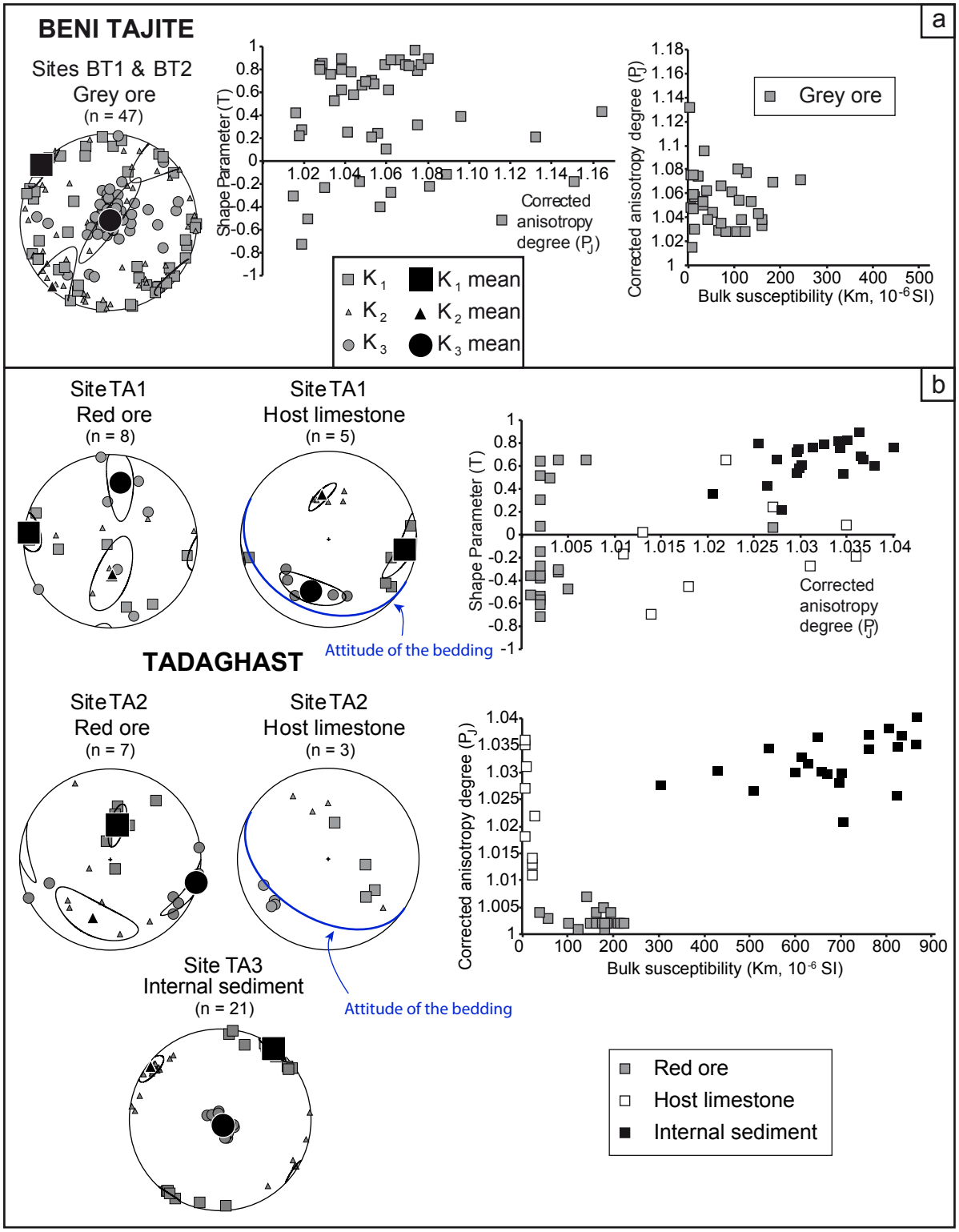

Figure 10

Figure 11

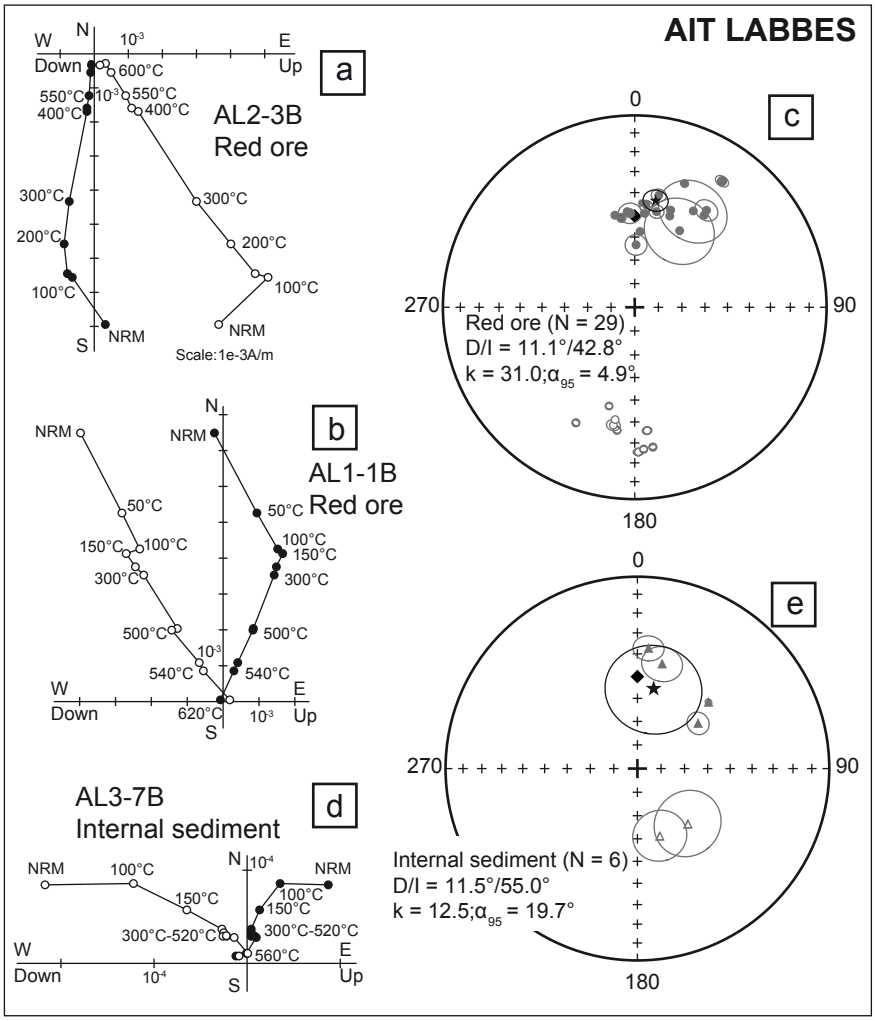

Figure11

Figure 12

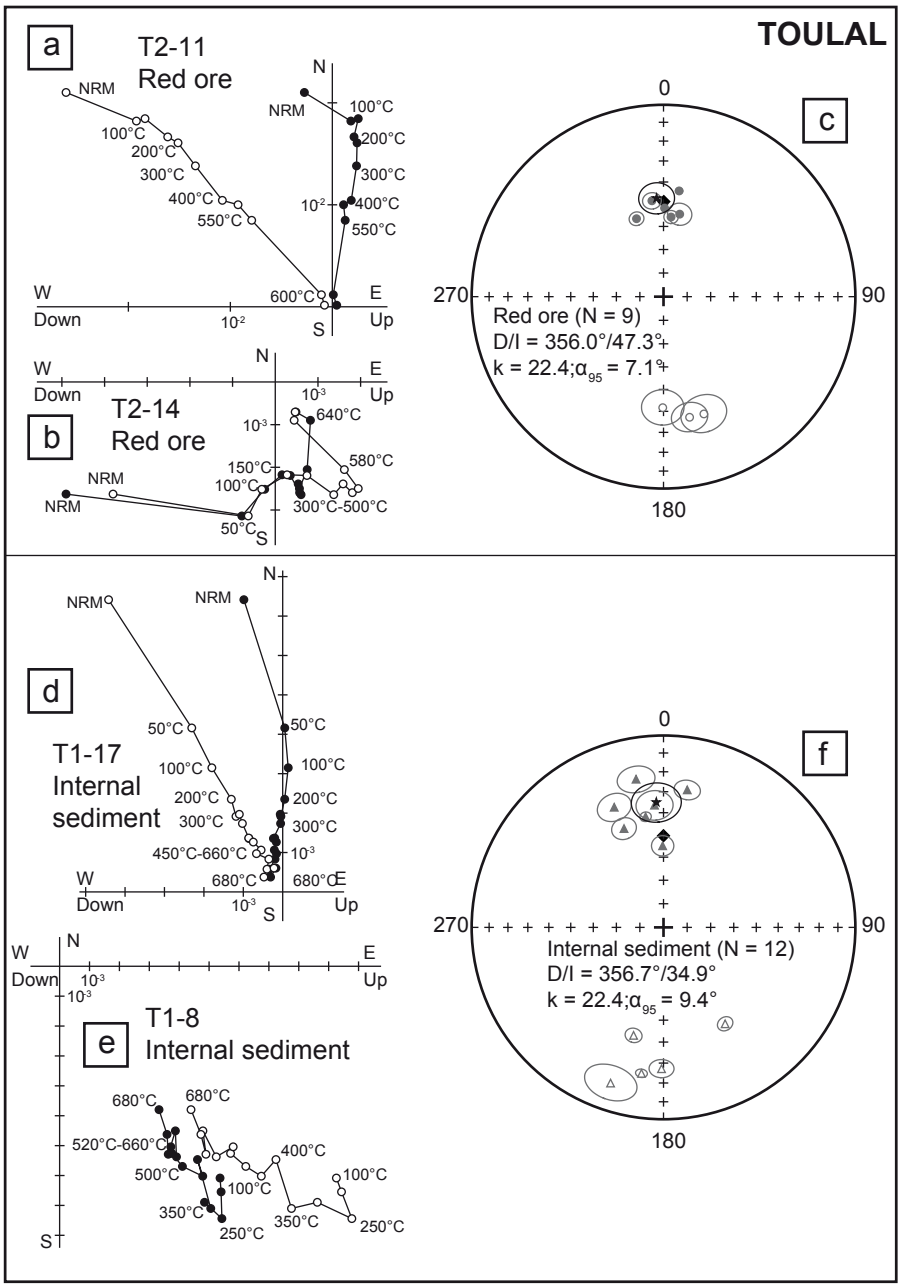

Figure 12

Figure 13

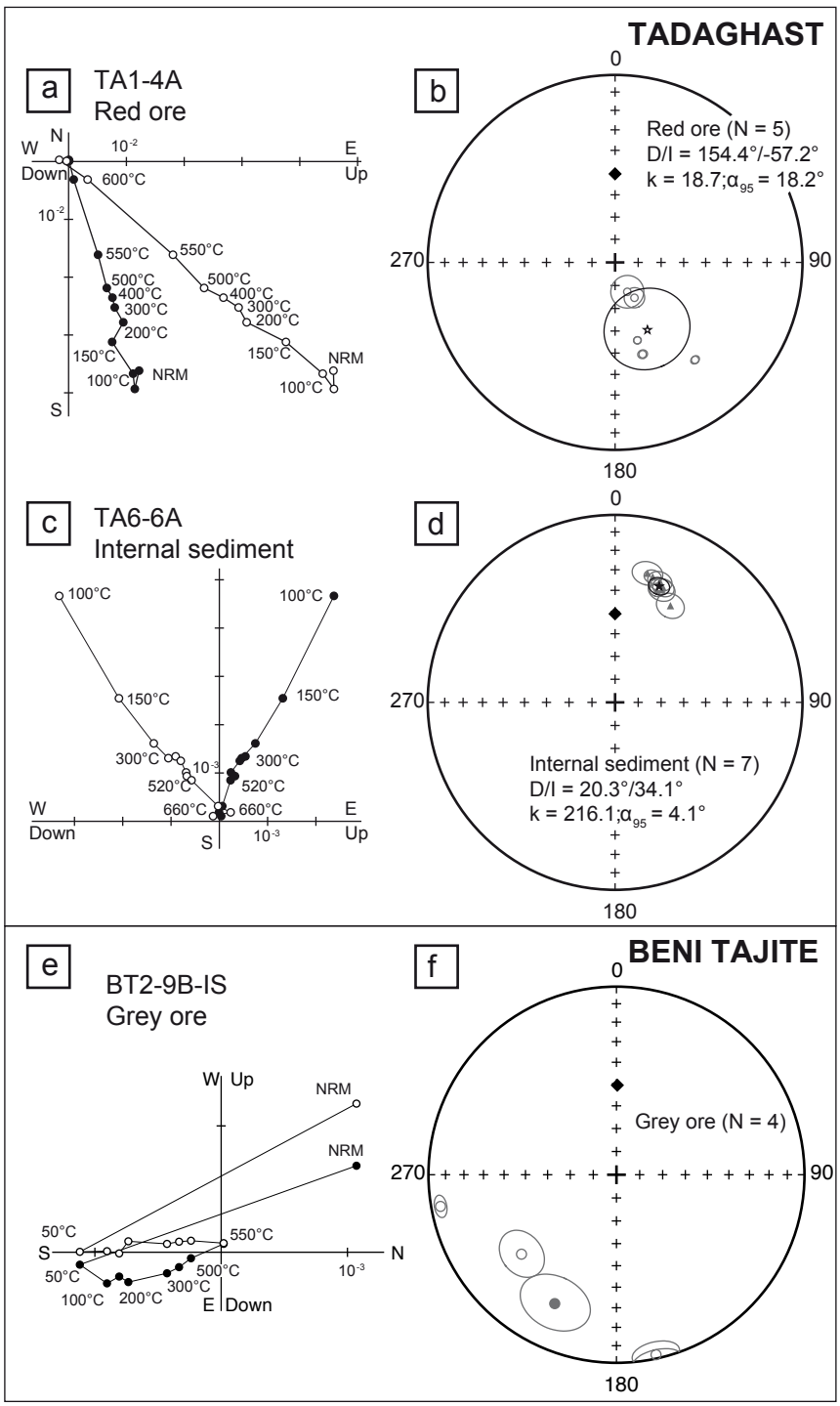

Figure 13

Figure 14

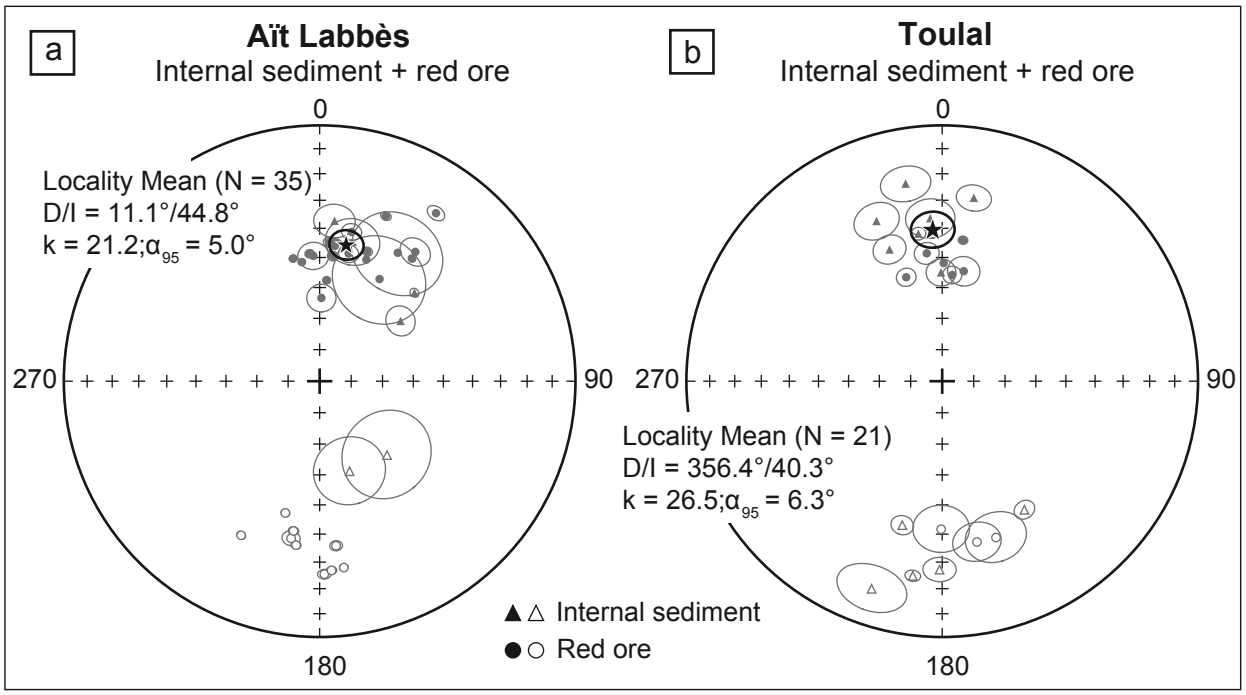

Figure 14

Figure 15

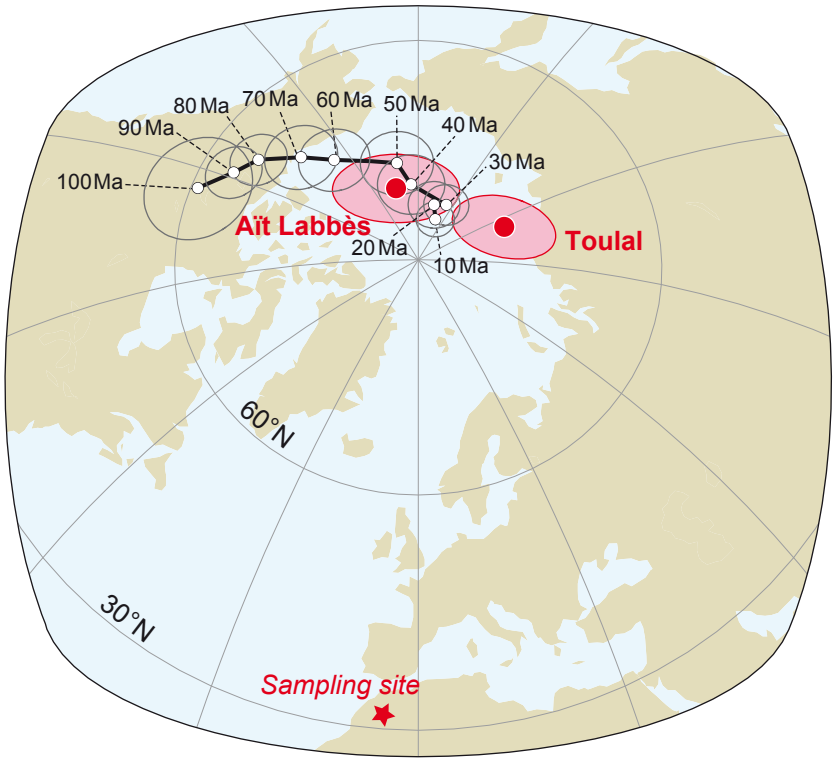

Figure 15

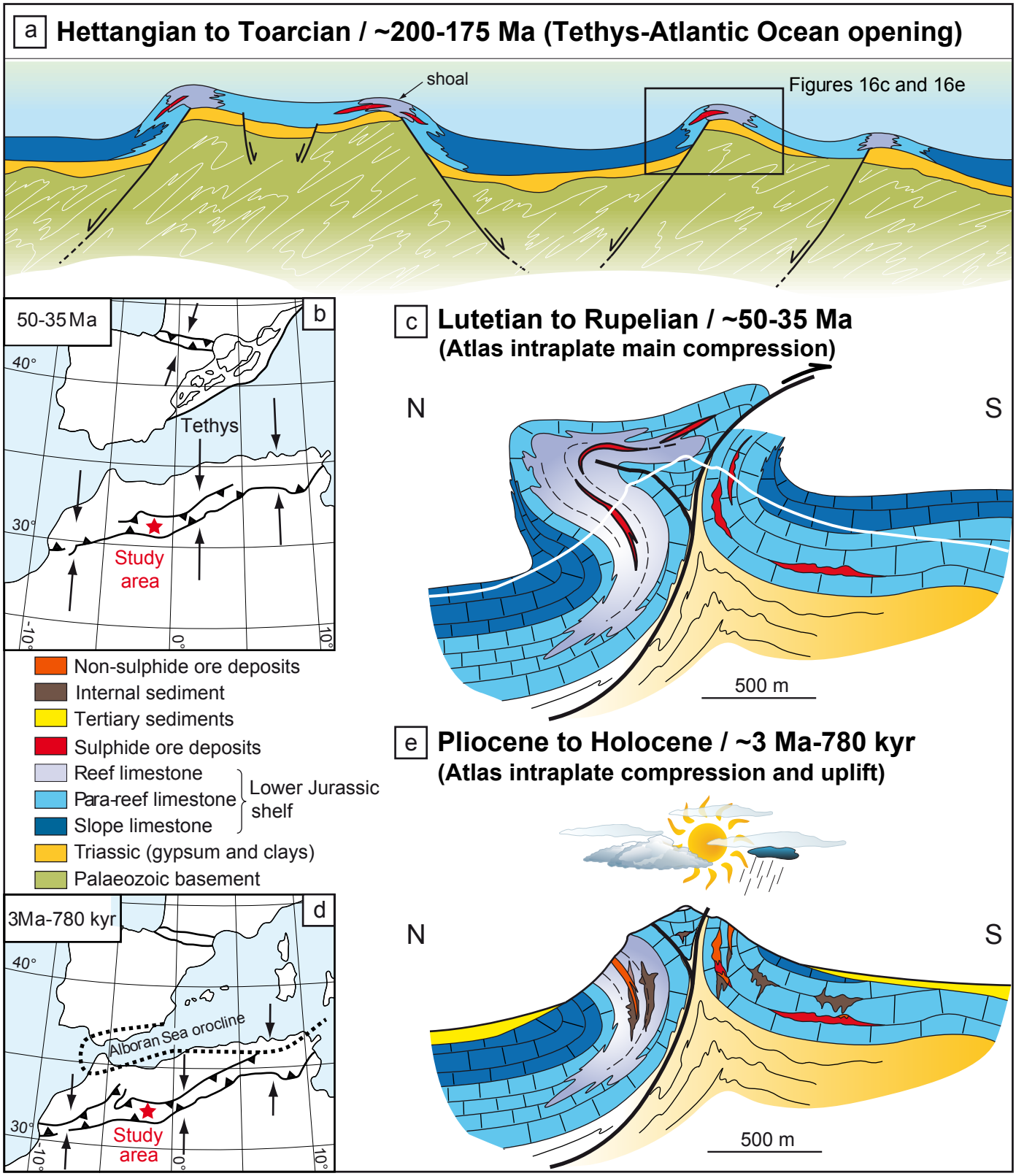
a
Hettangian to Toarcian / ~200-175 Ma (Tethys-Atlantic Ocean opening)
shoal
Figures 16c and 16e
50-35 Ma
b
40°
30°
Tethys
Study area
-10°
0°
10°
Non-sulphide ore deposits
Internal sediment
Tertiary sediments
Sulphide ore deposits
Reef limestone
Para-reef limestone
Slope limestone
Lower Jurassic shelf
Triassic (gypsum and clays)
Palaeozoic basement
3Ma-780 kyr
d
Alboran Sea orocline
c
Lutetian to Rupelian / ~50-35 Ma
(Atlas intraplate main compression)
N
S
500 m
e
Pliocene to Holocene / ~3 Ma-780 kyr
(Atlas intraplate compression and uplift)

Figure 16

Table 1

Table 1

Deposit	n/N	Km ($x10^{-6}$ SI)	P_J	T	K_1				K_2				K_3			
					D (°)	I (°)	α_{95max}	α_{95min}	D (°)	I (°)	α_{95max}	α_{95min}	D (°)	I (°)	α_{95max}	α_{95min}
Aït Labbès (N32.384°; W04.384°)																
AL1 - Red ore	21/26	13.5	1.001	0.051	232.1	27.1	49.2	20.9	357.0	48.2	49.4	21.5	125.5	29.1	23.1	21.0
AL1 - Host limestone	6/6	30.1	1.015	0.499	329.1	15.7	31.3	11.0	231.4	25.4	31.3	4.7	87.6	59.5	11.6	3.8
AL2 - Red ore	10/18	561.0	1.009	-0.183	317.8	48.9	24.6	17.1	70.4	18.6	21.2	11.0	174.1	35.1	25.2	15.2
AL3 - Internal sediment	16/19	40.1	1.004	-0.059	80.5	4.7	37.9	20.5	350.3	2.6	39.6	20.3	231.9	84.6	25.1	20.6
AL3 - Red ore	6(N)	*no calculation - scattered data*														
Toulal (N32.305°; W03.986°)																
T1 - Internal sediment	30/31	291.0	1.026	0.743	282.0	1.9	68.3	8.3	12.0	0.0	68.3	8.1	102.8	88.1	9.5	8.2
T2+T3 - Red ore	16/22	314.0	1.006	0.301	83.0	3.0	60.7	3.0	173.5	10.4	60.7	16.7	336.8	79.2	18.2	12.0
T1+T2+T3 - Host limestone	9/12	76.9	1.011	0.008	35.0	49.7	28.7	13.0	181.9	35.4	22.6	14.2	284.2	16.7	29.8	14.4
Beni Tajite (N32.302°; W03.451°)																
BT1/BT2 - Grey ore	47/49	49.3	1.035	0.391	310.8	0.1	18.6	9.4	220.8	2.2	48.9	12.7	44.0	87.8	48.4	8.4
Tadaghast (N31.636°; W06.606°)																
TA1 - Red ore	8/10	161.0	1.003	-0.361	276.0	5.8	17.4	10.9	177.0	57.3	37.8	15.0	9.6	32.1	37.3	10.6
TA1 - Host limestone	5/5	6.7	1.029	-0.109	97.7	13.9	28.5	7.8	351.3	48.9	17.2	4.9	198.8	37.8	29.4	12.2
TA2 - Red ore	7/11	180.0	1.002	-0.283	11.6	58.1	20.7	6.3	196.3	31.8	37.4	16.6	105.0	2.1	36.1	6.2
TA2 - Host limestone	3(N)	*no calculation - not enough data*														
TA3 - Internal sediment	21/21	695.0	1.033	0.641	36.8	2.4	11.4	3.7	306.6	5.1	11.4	8.2	152.0	84.4	8.7	4.1

Table 2

Site	n	D [°]	I [°]	MAD [°]
AIT LABBES				
Red ore				
AL1-12	9	34.7	21.2	2.5
AL1-14	9	1.2	63.4	4.5
AL1-1B	8	21.9	31.1	1.5
AL1-21A	4	30.4	51.8	14.4
AL1-4A	9	6.6	44.8	.0
AL1-4A	11	357.1	49.4	4.6
AL1-6A	8	21.0	47.8	.1
AL1-6A	10	12.8	47.6	3.0
AL2-12B	8	31.3	40.9	13.8
AL2-3B	8	178.6	-25.5	1.8
AL2-3B	9	188.2	-35.5	1.4
AL2-4B	10	190.3	-37.6	2.6
AL2-7	9	189.9	-40.3	1.5
AL2-7	10	194.6	-45.8	1.3
AL2-8B	8	37.0	39.8	1.1
AL2-8B	4	36.5	37.2	4.6
AL1-11	11	20.2	45.1	1.5
AL1-13A	10	6.0	49.3	1.6
AL1-13B	9	6.4	45.8	2.5
AL1-15B	9	4.0	57.5	1.2
AL1-5A	10	351.5	51.1	1.1
AL1-5B	10	347.8	49.4	1.2
AL1-6B	9	355.5	48.6	1.4
AL1-7	4	12.1	40.1	2.9
AL2-10A	10	3.9	44.7	1.7
AL2-10B	6	176.4	-26.8	1.4
AL2-2	9	207.0	-32.9	1.3
AL2-3A	6	174.3	-35.6	1.8
AL2-4A	3	172.6	-27.4	1.2
Mean	**N = 29; D/I = 11.1°/42.8°; k = 31.0; a_{95} = 4.9°**			
Internal sediment				
AL3-1A	7	47.0	48.0	1.4
AL3-5B	5	161.6	-59.6	11.1
AL3-6A	8	53.3	57.6	4.7
AL3-6C	4	137.6	-57.9	14.1
AL3-7A	8	5.3	37.1	5.9
AL3-7B	8	13.3	43.3	8.0
Mean	**N = 6; D/I = 11.5°/55.0°; k = 12.5; a_{95} = 19.7°**			

Site	n	D [°]	I [°]	MAD [°]
BENi TAJITE				
Grey ore				
BT1-11A	6	230.1	-34.5	9.8

Site	n	D [°]	I [°]	MAD [°]
TOULAL				
Red ore				
T2-1	15	353.1	48.3	3.7
T2-11	8	8.4	43.6	1.4
T2-13A	7	11.1	53.9	4.9
T2-13B	10	340.9	54.6	3.0
T2-14	4	161.0	-35.6	8.8
T2-14	4	180.4	-41.7	8.2
T2-4	5	.7	51.9	.7
T2-5	2	167.8	-35.9	6.9
T2-7	7	5.4	55.7	2.9
Mean	**N = 9; D/I = 356.0°/47.3°; k = 54.0; a_{95} = 7.1°**			
Internal sediment				
T3-15A	7	349.5	22.5	6.7
T3-3B	9	359.4	55.0	4.5
T3-4A	11	355.8	36.3	7.0
T3-2A	4	338.2	43.8	4.9
T3-4A	10	180.8	-27.2	4.5
T3-5A	8	337.7	32.8	6.5
T3-6B	8	198.8	-15.4	9.1
T1-17	10	9.8	28.1	4.8
T1-6A	10	188.6	-24.1	2.1
T1-7A	8	195.5	-41.2	3.3
T1-8	10	147.4	-40.1	3.1
T1-9	8	350.8	41.2	2.2
Mean	**N = 12; D/I = 356.7°/34.9°; k = 22.4; a_{95} = 9.4°**			

Site	n	D [°]	I [°]	MAD [°]
TADAGHAST				
Red ore				
TA1-2A	6	151.3	-72.5	4.4
TA1-2B	8	157.4	-76.2	7.1
TA1-3	7	140.6	-33.2	1.8
TA1-4A	9	163.3	-47.6	2.0
TA1-4B	10	164.0	-54.4	1.6
Mean	**N = 5; D/I = 154.4°/-57.2°; k = 18.7; a_{95} = 18.2°**			
Internal sediment				
TA6-2A	10	29.8	40.3	5.7
TA6-3A	8	20.4	36.4	2.9
TA6-3B	5	16.7	30.7	3.3
TA6-4B	10	20.3	31.7	4.7
TA6-5B	10	22.9	34.0	4.2
TA6-6A	9	22.5	35.3	5.3
TA6-7A	10	14.1	29.7	5.8
Mean	**N = 7; D/I = 20.3°/34.1°; k = 216.1; a_{95} = 4.1°**			